

NUMERICAL ANALYSIS OF GRAIN SIZE AND ORIENTATION EFFECTS
IN MICROSCALE COMPRESSION WITH CRYSTAL PLASTICITY

A THESIS SUBMITTED TO
THE GRADUATE SCHOOL OF NATURAL AND APPLIED SCIENCES
OF
MIDDLE EAST TECHNICAL UNIVERSITY

BY

MUHAMMET BATUHAN PAÇACI

IN PARTIAL FULFILLMENT OF THE REQUIREMENTS
FOR
THE DEGREE OF MASTER OF SCIENCE
IN
MECHANICAL ENGINEERING

DECEMBER 2025

Approval of the thesis:

**NUMERICAL ANALYSIS OF GRAIN SIZE AND ORIENTATION
EFFECTS IN MICROSCALE COMPRESSION WITH CRYSTAL
PLASTICITY**

submitted by **MUHAMMET BATUHAN PAÇACI** in partial fulfillment of the requirements for the degree of **Master of Science in Mechanical Engineering, Middle East Technical University** by,

Prof. Dr. Naci Emre Altun
Dean, **Graduate School of Natural and Applied Sciences** _____

Prof. Dr. Serkan Dağ
Head of the Department, **Mechanical Engineering** _____

Prof. Dr. Haluk Darendeliler
Supervisor, **Mechanical Engineering, METU** _____

Examining Committee Members:

Prof. Dr. Suat Kadioğlu
Mechanical Engineering, METU _____

Prof. Dr. Haluk Darendeliler
Mechanical Engineering, METU _____

Prof. Dr. Ulaş Yaman
Mechanical Engineering, METU _____

Assoc. Prof. Dr. Orkun Özşahin
Mechanical Engineering, METU _____

Prof. Dr. Can Çoğun
Mechatronics Engineering, Çankaya University _____

Date: 22.12.2025

I hereby declare that all information in this document has been obtained and presented in accordance with academic rules and ethical conduct. I also declare that, as required by these rules and conduct, I have fully cited and referenced all material and results that are not original to this work.

Name Last name : Muhammet Batuhan Paçacı

Signature :

ABSTRACT

NUMERICAL ANALYSIS OF GRAIN SIZE AND ORIENTATION EFFECTS IN MICROSCALE COMPRESSION WITH CRYSTAL PLASTICITY

Paçacı, Muhammet Batuhan
Master of Science, Mechanical Engineering
Supervisor: Prof. Dr. Haluk Darendeliler

December 2025, 80 pages

This thesis investigates the grain-scale deformation behavior of polycrystalline copper under uniaxial compression through a systematic crystal plasticity finite element method (CPFEM). The study aims to quantify how microstructural parameters; grain size, grain orientation, and their coupled interactions govern the macroscopic mechanical response. Representative polycrystalline models are generated with varying grain numbers and orientations to examine their effects on deformation. First, convergence studies are carried out to determine the appropriate mesh and representative volume element sizes. Single-crystal analyses demonstrate that mechanical response and hardening characteristics are primarily dictated by Euler angles. Polycrystalline simulations revealed Hall–Petch-type grain-size strengthening and confirmed that intergranular constraint increases flow stress relative to single crystals. Analyses for polycrystals, introducing controlled orientation variation in all grains and changes restricted to central grain orientations,

show that orientation effects diminish with decreasing grain size. The results demonstrate that the macroscopic response of polycrystalline copper arises from the combined effects crystallographic orientations and intergranular compatibility. It is observed CPFEM is capable of predicting the effects of grain size, grain orientation, and their coupling in face-centered cubic (FCC) metals.

Keywords: Crystal Plasticity, Grain Orientation, Grain Size Effect, Microstructure

ÖZ

TANE BOYUTU VE YÖNÜNÜN MİKRO ÖLÇEKLI BASMA ÜZERİNDEKİ ETKİLERİNİN KRİSTAL PLASTİSİTE İLE SAYISAL ANALIZI

Paçacı, Muhammet Batuhan
Yüksek Lisans, Makina Mühendisliği
Tez Yöneticisi: Prof. Dr. Haluk Darendeliler

Aralık 2025, 80 sayfa

Bu tez, çok kristalli bakırın tek eksenli basma altında tane ölçeğindeki şekil değiştirme davranışını, sistematik bir kristal plastisite sonlu elemanlar yöntemi ile incelemiştir. Çalışma, mikroyapı parametrelerinin; tane boyutu, tane yönü ve bunların birleşik etkileşimlerinin, makroskopik mekanik davranışı nasıl etkilediğini nicel olarak ortaya koymuştur. Farklı tane sayıları ve yönlerine sahip çok kristalli modeller oluşturulmuş ve deformasyon üzerindeki etkileri incelenmiştir. İlk olarak, uygun ağ ve temsili hacim elemanı boyutlarını belirlemek amacıyla yakınsama çalışmaları yürütülmüştür. Tek kristal analizleri, mekanik davranışın ve pekleşme karakteristiklerinin esas olarak Euler açıları tarafından belirlendiğini göstermiştir. Çok kristalli benzetimler, Hall–Petch tipi tane-boyutu dayanım artışını ortaya koymuş ve tanelerarası kısıtlamanın, tek kristallere kıyasla akma gerilmesini artırdığını teyit etmiştir. Tüm tanelerde kontrollü yön değişiminin uygulandığı ve yönelim değişimlerinin yalnızca merkezdeki tanelerle sınırlandırıldığı çok kristalli analizler, tane boyutu küçüldükçe yön etkilerinin azaldığını göstermiştir. Sonuçlar, çok kristalli bakırın makroskopik davranışının, kristalografik yönelimler ile

tanelerarası uyumluluğun birleşik etkilerinden kaynaklandığını ortaya koymuştur. Elde edilen bulgular, kristal plastisite sonlu elemanlar yönteminin, yüzey merkezli kübik yapıli metallerde tane boyutu, tane yönelimi ve bunların birleşik etkilerini öngörebildiğini göstermektedir.

Anahtar Kelimeler: Kristal Plastikliđi, Tane Yönelimi, Tane Boyutu Etkisi, Mikroyapı

To my beloved Dilara and my family

ACKNOWLEDGMENTS

I would like to express my deepest gratitude to Prof. Dr. Haluk Darendeliler for his invaluable guidance, continuous support, and profound insight throughout the course of this study. His expertise and mentorship have been instrumental in shaping both the academic and professional aspects of my research. I am sincerely thankful for his patience, trust, and inspiration, which have greatly contributed to the completion of this thesis.

This thesis represents not only the culmination of my academic journey, but also the foundation upon which I will continue to pursue scientific curiosity with discipline, integrity, and purpose.

TABLE OF CONTENTS

ABSTRACT.....	v
ÖZ.....	vii
ACKNOWLEDGMENTS.....	x
TABLE OF CONTENTS.....	xi
LIST OF TABLES.....	xiv
LIST OF FIGURES.....	xv
LIST OF ABBREVIATIONS.....	xviii
LIST OF SYMBOLS.....	xix
CHAPTERS	
1 INTRODUCTION.....	1
1.1 Background and Motivation.....	2
1.2 Objective of the Thesis.....	2
1.3 Scope of the Thesis.....	3
1.4 Outline of the Thesis.....	3
2 LITERATURE REVIEW.....	5
2.1 Foundation of Crystal Plasticity and Microstructural Sensitivity.....	5
2.2 Grain Boundaries as Active Plasticity Modulators.....	6
2.3 Gradient Micromorphic and Dislocation-Based CPFEM Models.....	7
2.4 Nanocrystalline and Ultrafine-Grained Regimes.....	8
2.5 State-of-the-Art and Emerging Research Directions.....	8
3 THEORY AND GOVERNING EQUATIONS.....	11
3.1 Theory of Crystal Plasticity.....	11

3.1.1	Kinematics	11
3.1.2	Constitutive Law	15
3.1.3	Hardening Law	18
3.1.4	Critical Resolved Shear Stress.....	19
3.1.5	Geometrically Necessary Dislocations.....	20
3.2	Crystalline Structures	21
3.2.1	Euler Bunge Angles.....	22
3.2.2	Schmid Factor Calculations.....	23
4	CRYSTAL PLASTICITY MODELING AND SIMULATION	
	FRAMEWORK	25
4.1	Finite Element Method	25
4.1.1	Forward Gradient Time Integration Scheme	26
4.1.2	Incremental Formulation	27
4.2	Polycrystal Generation	29
4.3	Meshing and Convergence Study	30
4.4	Boundary Conditions and Loading.....	32
4.5	Selected Material Information	33
5	RESULT AND DISCUSSION	35
5.1	Model Convergence – Sensitivity Analysis	36
5.1.1	Mesh Density.....	36
5.1.2	RVE Size	38
5.2	Grain Size Effect	40
5.3	Grain Orientation Effect.....	45
5.3.1	Single Crystal	46

5.3.2	Polycrystals	55
5.4	Coupled Effect of Orientation and Grain Size Variation.....	57
5.4.1	Grain Set Generation.....	57
5.4.2	Comparative Analysis Between $\pm 10^\circ$ and $\pm 20^\circ$	60
5.4.3	Comparative Analysis Between $\pm 10^\circ$ and $\pm 50^\circ$	61
5.5	Central Grain Orientation Effects	63
5.5.1	Central Grain Orientation for 50 Grain RVE Results	65
5.5.2	Central Grain Orientation for 500 Grains RVE Results	67
5.5.3	Comparison of Affected Regions 50 vs 500 Grains	70
6	CHAPTER 6 CONCLUSION.....	73
6.1	Grain Orientation Effects	73
6.2	Grain Size Effect.....	74
6.3	Coupled Orientation – Size Effect	74
6.4	Central Grain Orientation Effect.....	74
6.5	Overall Interpretation.....	75
6.6	Future Work	75
	REFERENCES	77

LIST OF TABLES

TABLES

Table 4.5-1 Selected Material Parameters of Cu for CPFEM	33
Table 5.1-1 True Stress Comparison at 0.2 Strain for Meshing Parameters	38
Table 5.2-1 Average Grain Size & Number of Grain Correlations.....	42
Table 5.2-2 The resulting flow stresses and stress levels at 10% strain for different grain size.....	44
Table 5.3-1 Schmid factors for single crystal with Euler angles of (0°, 45°, 45°)..	47
Table 5.3-2 Schmid factors for single crystal with Euler angles (324°, 108°, 98°)	49
Table 5.3-3 Max Schmid Factors for single crystals with different Euler Bunge angles	52
Table 5.3-4 True stress-strain at 10% strain for different Euler Bunge Angles	56
Table 5.4-1 Comparative analysis of 50 and 500 Grains for ±10° and ±20° standard deviations.....	61
Table 5.4-2 Comparative analysis of 50 and 500 Grains for ±10° and ±50° standard deviations.....	63

LIST OF FIGURES

FIGURES

Figure 3.1-1 Illustration of the kinematic response of a crystal undergoing elastic-plastic deformation via lattice slip mechanisms [22].	12
Figure 3.1-2 Initial and current coordinate representation of displaced particle	13
Figure 3.2-1 Scheme of crystal lattice structures of metals [18]	21
Figure 3.2-2 Slip system for an FCC lattice structure [19].	22
Figure 3.2-3 Schematic representation of Euler Bunge angle and its rotational for a cubic crystal [20].	23
Figure 3.2-4 Schematic representation of slip plane and slip direction for a specimen [21].	24
Figure 4.2-1 RVE created by Neper to be used in CPFEM simulation	29
Figure 4.3-1 Schematic representation of C3D10 Meshing Element	31
Figure 4.4-1 Boundary conditions and related Reference Points (RP) are represented.	33
Figure 5.1-1 RVE models with 6 different mesh density – rcl 0.1 to 0.6.	37
Figure 5.1-2 True stress true strain curves for 6 different mesh element sizes.....	37
Figure 5.1-3 Different RVE Sizes schematic view of 0.1 mm (blue), 1 mm (red), and 10 mm (green). The 0.1 mm model is highlighted in a box.....	39
Figure 5.1-4 True stress & strain curve for different RVE Sizes schematic view of 0.1 mm (blue), 1 mm (red), and 10 mm (green). %20 strain region is highlighted in right – below corner.	40
Figure 5.2-1 RVE models for a single crystal and polycrystals with 10, 100, 500 grains respectively	41
Figure 5.2-2 True stress-strain curves for different grain numbers in RVE.	42
Figure 5.2-3 Highlighted True stress-strain curves for different grain numbers in RVE.....	43
Figure 5.2-4 Closer look to the 0.2% strain for different number of grains.	43
Figure 5.2-5 Hall-Petch plot with curve fitting for $\sigma_y = \sigma_0 + kyd - 1/2$	45

Figure 5.3-1 Total accumulated slip (γ) contours for all twelve $\{111\}\langle 110\rangle$ slip systems, (a) to (l), for the Euler angle of $(0^\circ, 45^\circ, 45^\circ)$	48
Figure 5.3-2 True stress-strain plot for $(0^\circ, 45^\circ, 45^\circ)$ single crystal	49
Figure 5.3-3 Total accumulated slip (γ) contours for all twelve $\{111\}\langle 110\rangle$ slip systems, (a) to (l), for the Euler angle of $(324^\circ, 108^\circ, 98^\circ)$	50
Figure 5.3-4 True stress-strain comparison plot for the Euler angles of $(0^\circ, 45^\circ, 45^\circ)$ and $(324^\circ, 108^\circ, 98^\circ)$ single crystals	51
Figure 5.3-5 The corresponding true stress–true strain curves for all orientations	53
Figure 5.3-6 Two selected orientations true stress-strain curves for single crystals for lowest and highest true stresses	54
Figure 5.3-7 Presents the von Mises stress contours for the $(0^\circ, 55^\circ, 45^\circ)$ and $(324^\circ, 108^\circ, 98^\circ)$	54
Figure 5.3-8 True stress–true strain curves for different Euler angles for 500 Grains polycrystal	56
Figure 5.3-9 Total accumulated slip (γ) contours for all twelve $\{111\}\langle 110\rangle$ slip systems, (a) to (l), in $(0^\circ, 45^\circ, 45^\circ)$ for polycrystal	57
Figure 5.4-1 Max Schmid Factor histograms for three different standard deviation for 500 grains.....	59
Figure 5.4-2 Max Schmid Factor histograms for three different standard deviation for 50 grains.....	60
Figure 5.4-3 True stress–true strain curves for $\pm 10^\circ$ and $\pm 20^\circ$ standard deviations.....	61
Figure 5.4-4 True stress–true strain curves for $\pm 10^\circ$ and $\pm 50^\circ$ standard deviations.....	62
Figure 5.5-1 Max Schmid Factor histograms for four different standard deviation for 500 grains.....	64
Figure 5.5-2 Max Schmid Factor histograms for four different standard deviation for 50 grains.....	65
Figure 5.5-3 The overall geometries of the 50 (a), (c) and 500 (b), (d) grain RVEs	66

Figure 5.5-4 Section view cutted through central grain shows total equivalent plastic strain contours for (0°, 45°, 45°), (a) and (324°, 108°, 98°), (b) orientations for 50 grains. Arrows show significant local strain differences.	66
Figure 5.5-5 Full volume view shows total equivalent plastic strain contours for (0°, 45°, 45°), (a) and (324°, 108°, 98°), (b) orientations for 50 grains	67
Figure 5.5-6 Section view cutted through central grain shows Von Misses stress contours for (0°, 45°, 45°), (a) and (324°, 108°, 98°), (b) orientations for 50 grains	68
Figure 5.5-7 Section view cutted through central grain shows total equivalent plastic strain contours for (0°, 45°, 45°), (a) and (324°, 108°, 98°), (b) orientations for 500 grains. Arrows show significant local strain differences.	69
Figure 5.5-8 Full volume view shows total equivalent plastic strain contours for (0°, 45°, 45°), (a) and (324°, 108°, 98°), (b) orientations for 500 grains	70
Figure 5.5-9 Section view cutted through central grain shows Von Misses stress contours for (0°, 45°, 45°), (a) and (324°, 108°, 98°), (b) orientations for 500 grains	70
Figure 5.5-10 Section view cutted through central grain shows total equivalent plastic strain contours for (0°, 45°, 45°), (a), (c) and (324°, 108°, 98°), (b), (d) orientations for 50 and 500 grains with dashed circular region centered.	71

LIST OF ABBREVIATIONS

ABBREVIATIONS

CPFEM	Crystal Plasticity Finite Element Method
GB	Grain Boundary
TB	Twin Boundary
RVE	Representative Volume Element
FCC	Face-Centered Cubic
BCC	Body-Centered Cubic
HCP	Hexagonal Close-Packed
EBSD	Electron Backscatter Diffraction
GND	Geometrically Necessary Dislocation
SSD	Statistically Stored Dislocation
UMAT	User Material Subroutine
CZM	Cohesive Zone Model
CDRX	Continuous Dynamic Recrystallization
PEEQ	Equivalent Plastic Strain
AR	Aspect Ratio
RP	Reference Point
C3D10	10-node Quadratic Tetrahedral Element
SF	Schmid Factor

LIST OF SYMBOLS

SYMBOLS

ϕ_1, ϕ_2, Φ	Euler Angles in Bunge Convention
T	Transformation Matrix from Reference to Crystal Frame
τ_{cr}	Critical Resolved Shear Stress
F_a	Applied Force for Schmid Factor Representation
A	Area for Schmid Factor Representation
θ	Angle in Between Slip Plane Normal and Force Axis
λ	Angle in Between Slip Direction and Force Axis
m	Slip Plane Normal
s	Slip Direction
ζ	Intermediate Vector for Schmid Factor Calculation
X	Reference Coordinates
x	Current Coordinates
F	Deformation Gradient
*	Represents Elastic Components of Related Tensor
p	Represents Plastic Components of Related Tensor
v	Velocity Vector
L	Velocity Gradient
D	Stretching Rate
Ω	Spin Rate

$\boldsymbol{\mu}, \boldsymbol{\omega}$	Slip System Tensors
$\boldsymbol{\sigma}$	Cauchy Stress
$\boldsymbol{\tau}$	Kirchoff Stress
$\dot{\boldsymbol{\tau}}$	Material Rate of Kirchoff Stress
$\boldsymbol{\tau}^{\nabla^*}$	Jaumann Rate of Kirchoff Stress
\mathbb{C}	Elastic Stiffness Tensor with Tensor Symmetry
R	Special Transformation Matrix
\mathbb{C}_0	Elasticity Matrix for the Cubic Material in Crystal Reference
$\tau^{(\alpha)}$	Schmid Stress
ρ_0	Undeformed Configuration Density
ρ	Deformed Configuration Density
γ	Cumulative Shear Strain
$\dot{\gamma}$	Slip Rate
$\dot{\gamma}_0$	Strain Rate
g	Present State of Strain Hardening Within the Material
$h_{\alpha\beta}$	Slip Plane Latent Hardening Moduli
$h_{\alpha\alpha}$	Self-Hardening Moduli
τ_0	Yield Stress
h_0	Initial Hardening Modulus
q	Hardening Constant
g_0	Lattice Friction Stress
g_v	Voce Type Hardening

G	Shear Modulus
\mathbf{b}	Burger Vector
ξ	Geometric Factor
ρ_{GND}	Geometrically Necessary Dislocation Density
ρ_{tot}	Total Dislocation Density
\mathbf{n}	Edge Dislocation Line Direction
Λ	Lattice Incompatibility
ϵ_{ijk}	Levi-Civita Symbol

CHAPTER 1

INTRODUCTION

The need to use micro and nano sized materials and the steady increase in computational power and simulation capability over the last few decades has made it possible to investigate material behaviour at progressively smaller scales. Among these modelling approaches, crystal plasticity has become one of the most powerful tools for linking the macroscopic mechanical response of materials to their underlying microstructure. This framework enables the modelling of deformation at the level of individual grains, where anisotropy, slip activity, and grain interactions are explicitly represented. Compared to traditional continuum plasticity models, crystal plasticity formulations offer superior predictive accuracy and physical insight, particularly for metals with pronounced texture or heterogeneous grain structures.

In the context of metal forming and structural design, integrating crystal plasticity into numerical simulations can significantly improve the prediction of plastic flow, local stress concentrations, and damage initiation. Such understanding allows engineers to design lightweight and durable components by tailoring the microstructural configuration, namely, the grain size, orientation distribution, and grain boundary characteristics, toward optimal mechanical performance. In this thesis, the crystal plasticity finite element method (CPFEM) is employed to explore how microstructural attributes influence the deformation behaviour of polycrystalline metals. It provides a framework that bridges microscopic mechanisms and macroscopic material response.

1.1 Background and Motivation

The mechanical performance of polycrystalline metals is essentially governed by their microstructure. Traditional constitutive models often rely on empirical hardening laws, which average out the effects of grain-scale heterogeneities. While such approaches are computationally efficient, they fail to capture the true physics of deformation mechanisms that occur at the microscale, such as slip localization, grain boundary interactions, and orientation-dependent hardening.

Recent studies have demonstrated that even small variations in grain orientation or boundary misalignment can lead to significant differences in local strain distribution, which in turn influence macroscopic properties such as yield strength, ductility, and fatigue life. Therefore, a more fundamental approach that explicitly incorporates microstructural topology is essential for improving predictive capabilities in material design.

The motivation for this study arises from the need to quantify the role of grain boundary and orientation effects on the deformation behavior of metallic materials. With the increasing emphasis on simulation-driven design and virtual validation in industrial development, CPFEM has emerged as a practical tool that connects experimentally measurable microstructural parameters with computational predictions of stress–strain response. This thesis contributes to this ongoing effort by systematically investigating how variations in microstructural attributes affect the plastic response of a representative volume element (RVE) under compressive loading.

1.2 Objective of the Thesis

The primary objective of this research is to develop and apply a crystal plasticity-based computational framework to investigate the influence of microstructural parameters, particularly grain boundary characteristics, grain size, and grain orientation distribution, on the plastic deformation of polycrystalline metals.

The study aims to implement a CPFEM model capable of resolving grain-level deformation in a statistically representative microstructure, evaluate the impact of varying grain orientation spread and boundary arrangement on the overall mechanical response, quantify the relationship between microstructural heterogeneity and the evolution of stress and strain fields, and provide a physically grounded interpretation of how these parameters influence yielding and hardening behavior. Through this analysis, the work seeks to strengthen the link between microstructural design and macroscopic material performance, contributing to more predictive and physically consistent material models.

1.3 Scope of the Thesis

This thesis focuses on modelling the plastic deformation behaviour of copper under uniaxial compression using a crystal plasticity finite element approach. The computational framework includes; generation of 3D polycrystalline microstructures using Neper, mesh conversion for Abaqus simulations, integration of a crystal plasticity user material subroutine (UMAT) adapted from literature-based formulations, and simulation of various microstructural configurations to assess the effects of grain boundary density, grain size, and orientation dispersion on the overall response.

The scope is limited to quasi-static loading conditions, with emphasis on the plastic regime where slip activity and hardening mechanisms dominate. Thermal, creep, and dynamic effects are beyond the present focus. The results are intended to provide a mechanistic understanding rather than full-scale constitutive model calibration.

1.4 Outline of the Thesis

The thesis is organized into 6 chapters:

Chapter 1 presents the motivation, objectives, and overall scope of the study, emphasizing the significance of understanding grain-scale deformation in polycrystalline copper.

Chapter 2 summarizes previous research on crystal plasticity, grain boundary mechanics, and recent developments in CPFEM modeling frameworks.

Chapter 3 describes the theoretical foundation of crystal plasticity, including kinematics, constitutive and hardening laws, and the finite element formulation used in the simulations.

Chapter 4 details the generation of polycrystalline models, meshing strategy, boundary conditions, and material parameters adopted in the CPFEM implementation.

Chapter 5 presents and analyzes the simulation results, including mesh and RVE convergence, grain size and orientation effects, their coupling behavior, and local perturbation studies.

Chapter 6 summarizes the main findings, discusses their implications, and outlines potential directions for future research in grain-scale modeling of FCC metal.

CHAPTER 2

LITERATURE REVIEW

2.1 Foundation of Crystal Plasticity and Microstructural Sensitivity

The plastic deformation of crystalline metals fundamentally originates from the collective motion of dislocations and their interactions with internal interfaces such as grain boundaries (GBs), twin boundaries (TBs), and precipitates. Traditional continuum plasticity theories successfully described macroscopic yielding behavior but did not incorporate slip-system–based deformation mechanisms. The pioneering work of Asaro and Rice [1] established constitutive framework of crystal plasticity theory (CPT), formulating the relationship between slip-system-level shear stresses, critical resolved shear stresses, and crystal orientations within a finite strain setting. This seminal theory introduced a physically interpretable route to capture texture evolution and anisotropic hardening in microscale. Building on this theoretical foundation, Huang [2] implemented a single crystal plasticity UMAT in ABAQUS using both small- and finite-strain formulations, defining plastic flow through Schmid-law slip kinematics and incorporating multiple self- and latent-hardening relations. This computational framework established the basis for representing slip-system–controlled anisotropic deformation in later CPFEM studies.

To provide a theoretical link between such numerical formulations and the underlying lattice kinematics, Nye [3] introduced the dislocation density tensor, which quantifies lattice curvature and geometrically necessary dislocations (GNDs). This construction formalized how crystalline incompatibilities manifest as measurable continuum fields. Extending the theoretical framework, Arsenlis and Parks [4] proposed a constitutive model that explicitly describes the evolution of

statistically stored (SSDs) and GNDs. Their formulation remains central in modern CPFEM implementations by capturing Burgers-vector-conserving multiplication, annihilation, and interaction mechanisms. It also connects microstructural dislocation processes to macroscopic stress–strain behavior.

2.2 Grain Boundaries as Active Plasticity Modulators

Grain boundaries play a multifaceted role in dictating deformation behavior. Depending on their crystallographic misorientation, inclination, and energy, GBs can act as barriers, sinks, or emitters of dislocations. Experimental studies utilizing high-resolution EBSD and digital image correlation have revealed strain localization and lattice curvature concentration at GBs, underscoring their role as key drivers of heterogeneity in polycrystalline plasticity. Classical micromechanical experiments, such as the micro-bending tests performed by Jung et al. [5], have shown that the bending stiffness and flow behavior of thin polycrystalline metals strongly depend on the interaction between GBs and adjacent grains. Similarly, Espinosa et al. [6] interpreted size-scale plasticity by analyzing geometrically confined microstructures, concluding that the characteristic length associated with grain size and interface constraint dictates the hardening response. These findings highlighted the inadequacy of macroscopic constitutive laws that neglect boundary-induced gradients.

At smaller scales, Zhu et al. [7] demonstrated that interfacial plasticity governs strain-rate sensitivity and ductility in nanostructured metals. Their work revealed that coherent twin boundaries act as semi-permeable slip transmitters; they initially strengthen the material but progressively lose coherency, enhancing ductility through interface hardening. The mechanistic picture was further enriched by Dao, Lu, and Asaro [8], who provided a quantitative framework for nanocrystalline FCC metals, linking dislocation–boundary interactions, twin-mediated deformation, and dynamic grain growth to macroscopic stress–strain behavior.

2.3 Gradient Micromorphic and Dislocation-Based CPFEM Models

With the advancement of computational resources, CPFEM has become a primary tool for linking dislocation mechanics to macroscopic response. The early CPFEM implementations often treated GBs as geometrically perfect interfaces, neglecting intergranular slip transfer. Later, strain-gradient and micromorphic regularization techniques were introduced to incorporate non-local effects. Özdemir [9] outlined how gradient crystal plasticity models capture intragranular microstructure formation, while Cordero et al. [10] and Lindroos et al. [11] developed micromorphic formulations to introduce an internal length scale that penalizes high gradients in slip, thereby reproducing observed strain gradients near GBs.

The integration of physically based hardening mechanisms has also evolved. Haouala, Segurado, and Llorca [12] employed a dislocation-based CPFEM incorporating the Kocks–Mecking evolution law, explicitly accounting for dislocation storage at grain boundaries. Their simulations demonstrated that GBs are not merely kinematic boundaries but active regions influencing overall flow stress. Similarly, Petkov et al. [13] compared self-consistent and CPFEM frameworks for modeling high-temperature deformation in 316H steel, showing that grain-scale stress redistribution and boundary constraints critically affect creep resistance. These modern CPFEM approaches validate the necessity of grain-boundary-aware constitutive formulations to accurately predict strain localization, stress partitioning, and fatigue initiation.

Recent multiscale frameworks like Beyerlein et al. [14] further integrate texture evolution and dislocation accumulation under thermo-mechanical loads, revealing how GB-mediated incompatibilities govern macroscopic anisotropy. Such models lay the groundwork for next-generation CPFEM implementations, such as those by Demir et al. [15], which combine physically motivated hardening laws with interface-sensitive boundary conditions to capture strain localization and intergranular incompatibility in FCC metals.

2.4 Nanocrystalline and Ultrafine-Grained Regimes

Nanocrystalline metals exhibit unique deformation characteristics, where grain boundaries constitute a dominant fraction of the material volume. Dao, Lu, Asaro, and Ma [8] summarized how dislocation activity transitions toward GB-mediated mechanisms such as grain boundary sliding, rotation, and diffusional creep as grain size decreases below 100 nm. They demonstrated that the Hall–Petch relationship eventually inverts due to GB accommodation processes, giving rise to softening at extreme refinement.

Mishnaevsky and Schmauder [16] extended this concept through micromechanical modeling of nanocrystalline metals, showing that plastic flow becomes dominated by interface-mediated deformation rather than dislocation glide. Similarly, Bacca et al. [17] highlighted the interplay between continuous dynamic recrystallization (CDRX) and dislocation annihilation, suggesting that microstructural evolution during severe plastic deformation strongly modifies boundary structure and, hence, mechanical response. The integration of recrystallization kinetics into CPFEM remains an emerging research frontier, particularly relevant to cyclic or high-temperature deformation.

2.5 State-of-the-Art and Emerging Research Directions

Over decades of theoretical and computational advancements, crystal plasticity modeling has evolved into a robust framework for describing the deformation behavior of polycrystalline materials. However, despite the progress achieved in understanding slip system interactions and grain-scale heterogeneity, several key challenges persist:

- Quantitative Representation of Grain Boundary Constraints – While current CPFEM formulations can qualitatively reproduce grain-size strengthening, the explicit treatment of grain boundary constraint and slip transfer remains

limited. Developing boundary-sensitive formulations that can reproduce experimentally observed heterogeneity is an ongoing research frontier.

- Orientation-Driven Heterogeneity and Strain Localization – Recent findings highlight that even minor orientation deviations at the grain level can significantly influence local stress and strain partitioning. Capturing this sensitivity requires accurate initialization of grain orientation distributions and rigorous validation against experimentally derived textures.
- Scale Dependence and Statistical Convergence – The appropriate choice of RVE size and mesh resolution remains a central question in CPFEM. Establishing convergence criteria that ensure statistically meaningful yet computationally feasible simulations continue to be a practical challenge in microstructure-based modeling.

In this thesis, these challenges are addressed by systematically investigating the roles of grain orientation, grain size, and their coupled effects on the macroscopic and microscopic mechanical response of FCC copper. The adopted CPFEM framework builds upon the theoretical lineage of Asaro, Huang, and Demir, employing a physically grounded constitutive law that links slip system activation to experimentally calibrated material parameters. This approach enables a comprehensive yet computationally efficient evaluation of how microstructural morphology governs deformation behavior under uniaxial compression.

CHAPTER 3

THEORY AND GOVERNING EQUATIONS

3.1 Theory of Crystal Plasticity

Crystal plasticity theory offers a microscale formulation through which the evolution of slips on distinct crystallographic systems can be modeled. Unlike conventional continuum plasticity, crystal plasticity explicitly incorporates lattice orientation, slip-system geometry, and dislocation mechanics into the constitutive description. The resolved shear stress on each slip system governs the activation of plastic flow, while the hardening behavior is described through the evolution of dislocation densities and their interactions. This theoretical structure allows capturing orientation-dependent responses, grain size dependency and their combined effects to understand microstructure-sensitive behavior in polycrystals.

Total deformation is separated into an elastic lattice distortion and a plastic shear that occurs on discrete slip systems. The conceptual sequence of these mappings is illustrated in the Figure 3.1.1-1 below. Starting from the reference lattice, elastic deformation only contributes rotations and stretchings. Then plastic deformation is introduced through simple shearing along the slip direction $\mathbf{s}^{(\alpha)}$ on the plane with normal $\mathbf{m}^{(\alpha)}$. In this schematic, the evolution of the slip system basis between configurations highlights how shear strain $\gamma^{(\alpha)}$, slip-system activity, and lattice distortion jointly determine the anisotropic response of the crystal.

3.1.1 Kinematics

The coordinates X_i are called reference, material or Lagrangian coordinate and x_i coordinates are called current, spatial or Eulerian coordinates. As shown in the

Figure 3.1.1-2 below, a typical particle with position \mathbf{X} at time $t = t_0$ moves to position \mathbf{x} at time $t = t$. The motion of the particle can be described as

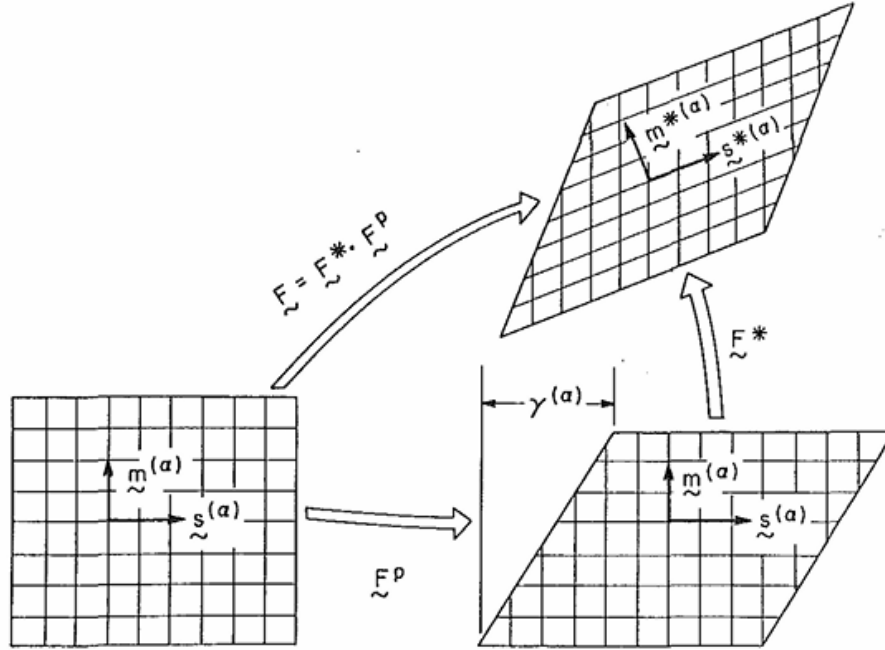


Figure 3.1-1 Illustration of the kinematic response of a crystal undergoing elastic-plastic deformation via lattice slip mechanisms [22].

$$\mathbf{x} = \mathbf{X} + \mathbf{u}$$

where \mathbf{u} is the displacement vector. In the cartesian coordinate system, the deformation gradient \mathbf{F} can be described as follows:

$$\mathbf{F} = \frac{\partial \mathbf{x}}{\partial \mathbf{X}}$$

and it can be decomposed into both elastic and plastic parts in absence of thermal effects:

$$\mathbf{F} = \mathbf{F}^* \cdot \mathbf{F}^P$$

where \mathbf{F}^* is deformation gradient component due to elastic stretch and rotation of the crystal lattice, \mathbf{F}^P is the slip-induced contribution to the overall deformation gradient. In the undeformed configuration $\mathbf{s}^{(\alpha)}$ represents the slip direction, whereas $\mathbf{m}^{(\alpha)}$ denotes the normal vector to the corresponding slip plane (α) [Fig.3.1-1]. Slip and

normal directions of the slip system $\mathbf{s}^{*(\alpha)}$ and $\mathbf{m}^{*(\alpha)}$ can be obtained from the undeformed configuration as:

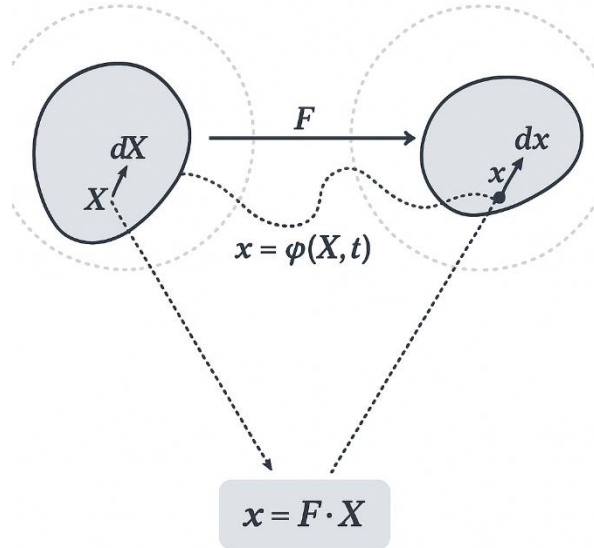


Figure 3.1-2 Initial and current coordinate representation of displaced particle

$$\mathbf{s}^{*(\alpha)} = \mathbf{F}^* \cdot \mathbf{s}^{(\alpha)}$$

$$\mathbf{m}^{*(\alpha)} = \mathbf{m}^{(\alpha)} \mathbf{F}^{*-1}$$

After deformation, $\mathbf{s}^{*(\alpha)}$ and $\mathbf{m}^{*(\alpha)}$ may change in length but stay orthogonal, satisfying:

$$\mathbf{s}^{*(\alpha)} \cdot \mathbf{m}^{*(\alpha)} = \mathbf{s}^{(\alpha)} \cdot \mathbf{m}^{(\alpha)} = 0$$

The velocity vector, \mathbf{v} , describes the material time derivative of the position vector and can be written as:

$$\mathbf{v} = \left(\frac{\partial \mathbf{x}}{\partial t} \right)_{\mathbf{X}}$$

The subscript \mathbf{X} implies that the reference position is fixed during differentiation. Hence, the time derivative corresponds to the motion of a material point in space. Velocity gradient in the current state can be written as:

$$\mathbf{L} = \dot{\mathbf{F}} \cdot \mathbf{F}^{-1} = \dot{\mathbf{F}}^* \cdot \mathbf{F}^{*-1} + \mathbf{F}^* \cdot \dot{\mathbf{F}}^P \cdot \mathbf{F}^{P-1} \cdot \mathbf{F}^{*-1} = \mathbf{D} + \mathbf{\Omega}$$

where the tensors \mathbf{D} is stretching rate, and $\mathbf{\Omega}$ is spin rate as given below. These tensors are symmetric, and skew-symmetric respectively, and their expressions in component form depend on the gradients of the \mathbf{v} , velocity field, across \mathbf{x} , spatial coordinates.

$$D_{ij} = \frac{1}{2} \left(\frac{\partial v_i}{\partial x_j} + \frac{\partial v_j}{\partial x_i} \right)$$

$$\Omega_{ij} = \frac{1}{2} \left(\frac{\partial v_i}{\partial x_j} - \frac{\partial v_j}{\partial x_i} \right)$$

They can also be decomposed in both elastic and plastic parts such as:

$$\mathbf{D} = \mathbf{D}^* + \mathbf{D}^P$$

$$\mathbf{\Omega} = \mathbf{\Omega}^* + \mathbf{\Omega}^P$$

where:

$$\mathbf{D}^P + \mathbf{\Omega}^P = \mathbf{F}^* \cdot \dot{\mathbf{F}}^P \cdot \mathbf{F}^{P-1} \cdot \mathbf{F}^{*-1}$$

Gradient of the plastic component of velocity vector, \mathbf{L}^P , can be described in terms of slipping rate for the slip system α as:

$$\mathbf{L}^P = \mathbf{D}^P + \mathbf{\Omega}^P = \sum_{\alpha=1}^n \dot{\gamma}^{(\alpha)} \mathbf{s}^{*(\alpha)} \otimes \mathbf{m}^{*(\alpha)}$$

Here $\mathbf{s}^{*(\alpha)} \otimes \mathbf{m}^{*(\alpha)}$ is called as Schmid Tensor. For the reference state lattice, the slipping rate is defined as follows:

$$\dot{\mathbf{F}}^P \cdot \mathbf{F}^{P-1} = \sum_{\alpha=1}^n \dot{\gamma}^{(\alpha)} \mathbf{s}^{(\alpha)} \otimes \mathbf{m}^{(\alpha)}$$

The plastic parts of the rate of stretching and the rate of spin tensors can be derived as follows:

$$\mathbf{D}^P = \sum_{\alpha=1}^n \dot{\gamma}^{(\alpha)} \left[\frac{1}{2} (\mathbf{s}^{*(\alpha)} \otimes \mathbf{m}^{*(\alpha)} + \mathbf{m}^{*(\alpha)} \otimes \mathbf{s}^{*(\alpha)}) \right]$$

$$\mathbf{\Omega}^P = \sum_{\alpha=1}^n \dot{\gamma}^{(\alpha)} \left[\frac{1}{2} (\mathbf{s}^{*(\alpha)} \otimes \mathbf{m}^{*(\alpha)} - \mathbf{m}^{*(\alpha)} \otimes \mathbf{s}^{*(\alpha)}) \right]$$

Let's denote

$$\mathbf{P}^{(\alpha)} = \frac{1}{2} (\mathbf{s}^{*(\alpha)} \otimes \mathbf{m}^{*(\alpha)} + \mathbf{m}^{*(\alpha)} \otimes \mathbf{s}^{*(\alpha)})$$

$$\mathbf{W}^{(\alpha)} = \frac{1}{2} (\mathbf{s}^{*(\alpha)} \otimes \mathbf{m}^{*(\alpha)} - \mathbf{m}^{*(\alpha)} \otimes \mathbf{s}^{*(\alpha)})$$

Then,

$$\mathbf{D}^P = \sum_{\alpha=1}^n \dot{\gamma}^{(\alpha)} \mathbf{P}^{(\alpha)}$$

$$\mathbf{\Omega}^P = \sum_{\alpha=1}^n \dot{\gamma}^{(\alpha)} \mathbf{W}^{(\alpha)}$$

where $\mathbf{P}^{(\alpha)}$ captures the contribution of slip to the plastic stretching, $\mathbf{W}^{(\alpha)}$ describes the associated spin generated by shear on system α . Together, these quantities provide a compact representation of how crystallographic slip influences the evolution of the deformation gradient through both shape change and lattice rotation. As plastic flow is fully governed by the slip rates $\dot{\gamma}^{(\alpha)}$, these tensorial measures form the bridge between microscale slip activity and the macroscopic stress response. Building on this kinematic structure, the constitutive formulation can now be introduced by relating the rate measures to the Kirchhoff stress and defining the elastic response of the lattice within the crystal plasticity framework.

3.1.2 Constitutive Law

The Kirchhoff stress tensor, $\boldsymbol{\tau}$ is defined as:

$$\boldsymbol{\tau} = j\boldsymbol{\sigma}$$

where, $j = \det(\mathbf{F})$ is the local volume change and $\boldsymbol{\sigma}$ is the Cauchy stress tensor.

According to Asaro [22] it is assumed that slip does not affect crystal elasticity, and the elastic constitutive law can be described as [18]:

$$\boldsymbol{\tau}^{\nabla*} = \mathbb{C} : \mathbf{D}^*$$

where $\boldsymbol{\tau}^{\nabla*}$ is the Jaumann rate of elastic Kirchoff stress and \mathbb{C} is the elastic stiffness tensor with tensor symmetry. To express the elastic response in the global frame, each grain's lattice orientation must be mapped from its local crystal coordinate system to the macroscopic reference frame. This coordinate transformation is performed using the Bond-type transformation matrix \mathbf{R} , which encodes the direction cosines of the crystal axes with respect to the sample axes. In this way, the anisotropic elastic properties specific to each grain orientations are consistently transferred into the global representation of the constitutive model. The explicit definition of the transformation matrix is presented in following section 3.2.1. According to the Demir et. al [15] the elastic stiffness tensor in the sample frame is obtained as follows:

$$\mathbb{C} = \mathbf{R}\mathbb{C}_0\mathbf{R}^T$$

where \mathbb{C}_0 is the elasticity matrix for the cubic material in the crystal reference, and defined with as follows:

$$\mathbb{C}_0 = \begin{bmatrix} C_{11} & C_{12} & C_{12} & 0 & 0 & 0 \\ C_{12} & C_{11} & C_{12} & 0 & 0 & 0 \\ C_{12} & C_{12} & C_{11} & 0 & 0 & 0 \\ 0 & 0 & 0 & C_{44} & 0 & 0 \\ 0 & 0 & 0 & 0 & C_{44} & 0 \\ 0 & 0 & 0 & 0 & 0 & C_{44} \end{bmatrix}$$

where C_{11} , C_{12} , and C_{44} are elastic stiffness constants of a cubic crystal. The Jaumann stress rate $\boldsymbol{\tau}^{\nabla*}$ describes the corotational change of stress on axes rotating with the lattice and can be described as follows:

$$\boldsymbol{\tau}^{\nabla*} = \dot{\boldsymbol{\tau}} - \boldsymbol{\Omega}^* \cdot \boldsymbol{\tau} + \boldsymbol{\tau} \cdot \boldsymbol{\Omega}^*$$

where $\dot{\boldsymbol{\tau}}$ is the material rate of Kirchoff Stress, and it can be linked to the equivalent stress rate on axes rotating with the material.

$$\boldsymbol{\tau}^{\nabla} = \dot{\boldsymbol{\tau}} - \boldsymbol{\Omega} \cdot \boldsymbol{\tau} + \boldsymbol{\tau} \cdot \boldsymbol{\Omega}$$

Building on this kinematic description, the next step is to relate the stress state to the driving forces for crystallographic slip. In crystal plasticity, these driving forces are expressed through the resolved shear stress acting on each slip system α . This quantity is obtained by projecting the Kirchhoff stress tensor onto the slip direction and slip-plane normal in the intermediate configuration, while accounting for the ratio of deformed to undeformed mass densities. Accordingly, the resolved shear stress on system α is written as

$$\tau^{(\alpha)} = \mathbf{m}^{*(\alpha)} \cdot \frac{\rho_0}{\rho} \boldsymbol{\tau} \cdot \mathbf{s}^{*(\alpha)}$$

where mass densities in the undeformed and deformed configuration are ρ_0 and ρ , respectively. Crystalline slip is considered to follow Schmid's law. Accordingly, the slip rate on a given system α is assumed to depend only on Schmid stress, $\tau^{(\alpha)}$, which reduces to the resolved shear stress when elastic distortions are negligible. Under conditions of finite elastic distortions, several generalizations exist, as noted for instance by Asaro and Rice [1]. In the thesis, the formulation is based on Huang Crystal Plasticity Finite Element Analysis framework [3]. Schmid stress's rate of change is given as:

$$\dot{\tau}^{(\alpha)} = \mathbf{m}^{*(\alpha)} \cdot [\boldsymbol{\tau}^{\nabla*} + \boldsymbol{\tau}(\mathbf{I}:\mathbf{D}^*) - \mathbf{D}^* \cdot \boldsymbol{\tau} + \boldsymbol{\tau} \cdot \mathbf{D}^*] \cdot \mathbf{s}^{*(\alpha)}$$

The evolution of the Schmid stress provides the driving force for slip activity on each crystallographic system. To fully characterize plastic flow, the Schmid stress must be linked with slip rate by a hardening law that governs how slip resistance evolves with accumulated deformation.

3.1.3 Hardening Law

According to Peirce, et. Al [25], the framework of rate-independent plasticity may be viewed as the limiting form of a rate-dependent viscoplastic model. In a rate-sensitive crystalline material, the slip rate $\dot{\gamma}^{(\alpha)}$ for system α is determined by the resolved shear stress $\tau^{(\alpha)}$ according to Schmid's law. According to Hutchinson [26] and Asaro [22], the slip rate is expressed by the following governing law:

$$\dot{\gamma}^{(\alpha)} = \dot{\gamma}_0^{(\alpha)} \left(\frac{\tau^{(\alpha)}}{g^{(\alpha)}} \right) \left| \frac{\tau^{(\alpha)}}{g^{(\alpha)}} \right|^{\left(\frac{1}{m}\right)-1}$$

In this relation, $\dot{\gamma}_0^{(\alpha)}$ is the reference strain rate, and $g^{(\alpha)}$ represents the current strength of material. Asaro [22] developed a hardening rule that accounts for the increase in slip resistance during progressive deformation specifically for the Voce-type hardening:

$$g_v^{(\alpha)} = \sum_{\beta=1}^n h_{\alpha\beta} \dot{\gamma}^{(\beta)}$$

where g_v represents Voce-type hardening, $h_{\alpha\beta}$ represents slip-plane hardening moduli. The summation is taken over all active slip systems. In this context, $h_{\alpha\alpha}$ (no summation implied) is self-hardening and $h_{\alpha\beta}$ ($\alpha \neq \beta$) is latent hardening moduli. Thus, self-hardening moduli, $h_{\alpha\alpha} = h(\gamma)$ can be described as follows according to Asaro [22], [27]:

$$h(\gamma) = h_0 \operatorname{sech}^2 \left| \frac{h_0 \gamma}{\tau_s - \tau_0} \right|$$

$h(\gamma)$ denotes the Voce-type self-hardening function. It starts from h_0 at zero plastic strain and decays towards zero as γ increases, reflecting saturation of hardening, where h_0 is the initial hardening modulus, and τ_0 is the yield stress, equal to the initial strength $g^{(\alpha)}(0)$ of the system. The value τ_s identifies the threshold stress

where intense plastic deformation starts. The term γ indicates the cumulative shear strain, summed over all slip systems following Taylor's approach as:

$$\gamma = \sum_{\alpha} \int_0^t |\dot{\gamma}^{(\alpha)}| dt$$

To describe the latent hardening moduli:

$$h_{\alpha\beta} = qh(\gamma) \quad (\alpha \neq \beta)$$

Here q is a constant. These formulations of the hardening moduli omit the influence of the Bauschinger effect which is a phenomenon observed in crystalline solids during cyclic reverse loading.

3.1.4 Critical Resolved Shear Stress

Following representation of the current strength $g^{(\alpha)}$ incorporates the influence of all relevant state variables on slip resistance. These include the lattice friction stress g_0 , phenomenological Voce-type hardening g_v , shear Modulus G , Taylor hardening characterized by a geometric factor α and the total dislocation density ρ_{tot} [15].

$$g^{(\alpha)} = g_0 + g_v + Gb^{(\alpha)}\sqrt{\xi^2\rho_{tot}}$$

The total dislocation density is obtained through appropriate projection operations that account for the geometrically necessary dislocations (GNDs) of edge and screw types, with their respective line directions denoted as $\mathbf{n}_e^{(b)}$ and $\mathbf{s}_s^{(b)}$

$$\rho_{tot}^a = \sum_b \left| \mathbf{m}^{(a)} \cdot \mathbf{n}_e^{(b)} \right| |\rho_{GND,e}^b| + \left| \mathbf{m}^{(a)} \cdot \mathbf{s}_s^{(b)} \right| |\rho_{GND,s}^b|$$

Subscripts e and s denote the edge and screw components of the geometrically necessary dislocation density, respectively. In this formulation, the statistically stored dislocation (SSD) density is not evaluated separately, since the Voce-type hardening law inherently reflects the averaged effect of dislocation accumulation

through its saturation response. Hence, no explicit dislocation evolution law is introduced, and the overall dislocation content is described only via the GND-related forest interactions, ensuring coherence with the phenomenological nature of the model.

3.1.5 Geometrically Necessary Dislocations

In the absence of defects such as cracks or voids, any lattice incompatibility is accommodated by geometrically necessary dislocations (GNDs). Nye [3] introduces an incompatibility tensor, $\mathbf{\Lambda}$ which provides a direct link to the densities of both screw and edge dislocations within each slip system. Das et. al [28] modified it as follows:

$$\mathbf{\Lambda} = -(\nabla \times \mathbf{F}^p)^T$$

where ∇ represent the gradient operator

$$\Lambda_{lk} = -\epsilon_{ijk}(F^p)_{lj,i}$$

where ϵ_{ijk} is the levi Civita operator. Decomposition of the incompatibility tensor into edge, $\rho_{GND_e}^{(\alpha)}$, and screw, $\rho_{GND_s}^{(\alpha)}$, dislocation densities can be shown as follows:

$$\mathbf{\Lambda} = \sum_{\alpha} \rho_{GND_e}^{(\alpha)} b^{(\alpha)} \mathbf{s}^{(\alpha)} \otimes \mathbf{n}^{(\alpha)} + \rho_{GND_s}^{(\alpha)} b^{(\alpha)} \mathbf{s}^{(\alpha)} \otimes \mathbf{s}^{(\alpha)}$$

where $b^{(\alpha)}$ is the magnitude of the Burger vector. Edge dislocation line direction $\mathbf{n}^{(\alpha)}$ is derived as:

$$\mathbf{n}^{(\alpha)} = \mathbf{s}^{(\alpha)} \times \mathbf{m}^{(\alpha)}$$

Relation in between incompatibility a dislocation density via the projection matrix $[\mathbf{A}]$:

$$\{\mathbf{\Lambda}\} = [\mathbf{A}]\{\rho_{GND}\}$$

Hence, Geometrically Necessary Dislocation can be computed as:

$$\{\rho_{\text{GND}}\} = (\mathbf{A}^T \mathbf{A})^{-1} \mathbf{A}^T \{\Lambda\}$$

Here, for slip system b , \mathbf{n}_b describes the line direction of an edge dislocation. It is determined as the cross product of the slip direction \mathbf{s}_b and the slip plane normal \mathbf{m}_b

3.2 Crystalline Structures

Crystalline solids are defined by the periodic arrangement of atoms within a lattice. The geometry of the repeating unit cell governs fundamental material properties such as density, slip behavior, and deformation mechanisms. Most commonly metallic systems can be described in three arrangements: face-centered cubic (FCC), body-centered cubic (BCC), and hexagonal close-packed (HCP) where these arrangements are shown in Figure 3.2-1:

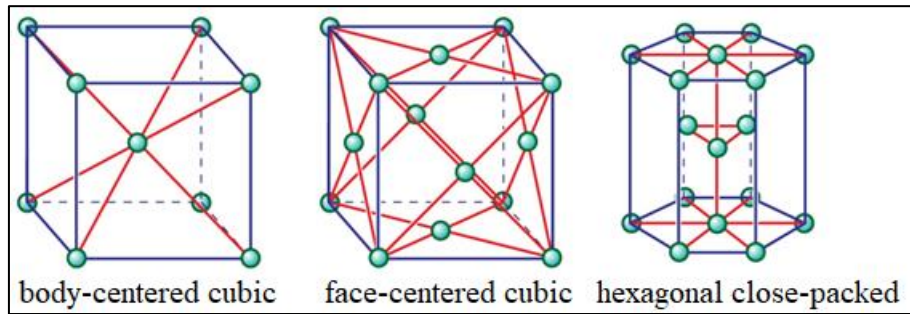


Figure 3.2-1 Scheme of crystal lattice structures of metals [18]

Since in this thesis copper, a material with an FCC crystal structure is used, the FCC lattice is described in detail to establish a solid foundation for the subsequent analyses. In an FCC lattice, atoms occupy both the cube corners and the centers of their faces. It yields a coordination number of 12 and an atomic packing factor of approximately 0.74. The densely packed $\{111\}$ planes and $\langle 110 \rangle$ slip directions provide numerous equivalent slip systems. The related slip systems can be seen in Fig 3.2-2. Therefore, it explains the high ductility and relatively low critical resolved shear stress observed in copper. This crystallographic background forms the basis for interpreting the CPFEM simulations presented in this work, particularly in

relation to slip system activation, dislocation density evolution, and the accumulation of localized strain near grain boundaries.

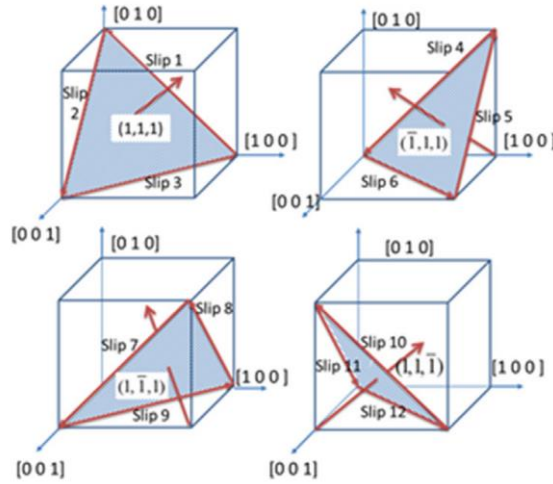


Figure 3.2-2 Slip system for an FCC lattice structure [19]

3.2.1 Euler Bunge Angles

Euler–Bunge angles provide a standardized way to describe the orientation of a crystal lattice relative to a fixed reference frame. They are defined by a sequence of three rotations, ϕ_1 , Φ , ϕ_2 . They capture how the crystal coordinate system is transformed from the sample coordinate system. ϕ_1 , Φ , ϕ_2 denotes rotations around the z , then rotation about x' in the rotated coordinate system and turn z'' axes after the second rotation, respectively, and it can be seen in Fig 3.2-3. This convention is widely used in texture analysis and crystallography because it enables consistent comparison of grain orientations across different measurements and models.

Let the T denote the transformation matrix from the reference sample coordinate system to crystal frame, obtained using the Euler angles according to the Bunge convention, then

$$T = \begin{bmatrix} \cos\phi_1\cos\phi_2 - \sin\phi_1\sin\phi_2\cos\Phi & \sin\phi_1\cos\phi_2 + \cos\phi_1\sin\phi_2\cos\Phi & \sin\phi_2\sin\Phi \\ -\cos\phi_1\sin\phi_2 - \sin\phi_1\cos\phi_2\cos\Phi & -\sin\phi_1\sin\phi_2 + \cos\phi_1\cos\phi_2\cos\Phi & \cos\phi_2\sin\Phi \\ \sin\phi_1\sin\Phi & -\cos\phi_1\sin\Phi & \cos\Phi \end{bmatrix}$$

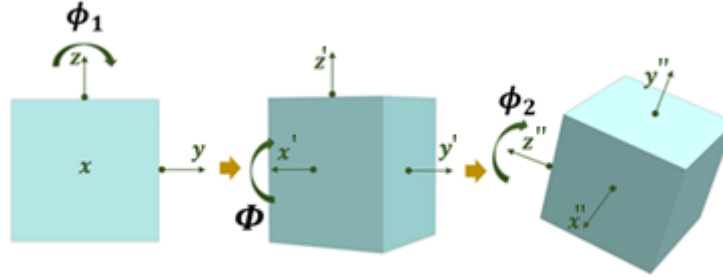


Figure 3.2-3 Schematic representation of Euler Bunge angle and its rotational for a cubic crystal [20]

And the rotation matrix, \mathbf{R} , is determined by using transformation matrix \mathbf{T} as follows [23]:

$$\mathbf{R} = \begin{bmatrix} (T_{11}^T)^2 & (T_{12}^T)^2 & (T_{13}^T)^2 & 2T_{11}^T T_{12}^T & 2T_{13}^T T_{11}^T & 2T_{12}^T T_{13}^T \\ (T_{21}^T)^2 & (T_{22}^T)^2 & (T_{23}^T)^2 & 2T_{21}^T T_{22}^T & 2T_{23}^T T_{21}^T & 2T_{22}^T T_{23}^T \\ (T_{31}^T)^2 & (T_{32}^T)^2 & (T_{33}^T)^2 & 2T_{31}^T T_{32}^T & 2T_{33}^T T_{31}^T & 2T_{32}^T T_{33}^T \\ T_{11}^T T_{21}^T & T_{12}^T T_{22}^T & T_{13}^T T_{23}^T & T_{11}^T T_{22}^T + T_{12}^T T_{21}^T & T_{13}^T T_{21}^T + T_{11}^T T_{23}^T & T_{12}^T T_{23}^T + T_{13}^T T_{22}^T \\ T_{31}^T T_{11}^T & T_{32}^T T_{12}^T & T_{33}^T T_{13}^T & T_{11}^T T_{32}^T + T_{12}^T T_{31}^T & T_{13}^T T_{31}^T + T_{11}^T T_{33}^T & T_{12}^T T_{33}^T + T_{13}^T T_{32}^T \\ T_{21}^T T_{31}^T & T_{22}^T T_{32}^T & T_{23}^T T_{33}^T & T_{22}^T T_{31}^T + T_{21}^T T_{32}^T & T_{21}^T T_{33}^T + T_{23}^T T_{31}^T & T_{22}^T T_{33}^T + T_{23}^T T_{32}^T \end{bmatrix}$$

3.2.2 Schmid Factor Calculations

The Schmid factor quantifies the effects of external load which can activate slip in each crystallographic system. It provides a direct measure of how microstructural characteristics influence plastic deformation through the orientation of a grain. In this work, Schmid factor is evaluated in order to utilize for understanding orientation-dependent mechanical responses. For a general stress state:

$$\tau_{cr} = \mathbf{m} \cdot \frac{\rho_0}{\rho} \boldsymbol{\tau} \cdot \mathbf{s}$$

Consider the uniaxial loading of a specimen given in Fig. 3.2-4, then [21]:

$$\tau_{cr} = \sigma \cos \lambda \cos \theta$$

where θ is the angle in between slip plane normal and force axis, and λ is the angle in between slip direction and force axis. Here, $\cos\lambda\cos\theta$ is called as Schmid factor, SF.

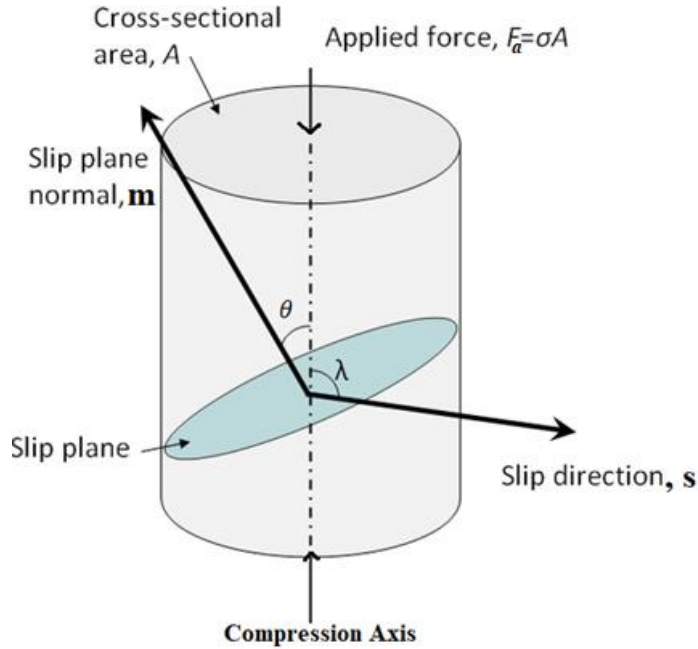


Figure 3.2-4 Schematic representation of slip plane and slip direction for a specimen [21]

For the grains whose coordinates do not coincide with specimen coordinates, the coordinate transformation is needed by using transformation matrix T :

$$\boldsymbol{\zeta} = T \cdot \mathbf{u}_a$$

where \mathbf{u}_a is the unit vector in the direction of applied load and $\boldsymbol{\zeta}$ is an intermediate vector, then

$$\cos\theta = \boldsymbol{\zeta} \cdot \mathbf{m}$$

$$\cos\lambda = \boldsymbol{\zeta} \cdot \mathbf{s}$$

Hence, Schmid Factor SF can be calculated accordingly:

$$SF = \cos\theta\cos\lambda$$

CHAPTER 4

CRYSTAL PLASTICITY MODELING AND SIMULATION FRAMEWORK

4.1 Finite Element Method

In this thesis, to obtain numerical results of the mechanical response of the FCC copper under imposed boundary conditions, the Finite Element Method (FEM) is utilized. It is a numerical technique used to obtain approximate solutions to boundary value problems governed by partial differential equations. By discretizing a continuum body into a collection of finite elements which are associated with interpolation functions, material laws, and nodal degrees of freedom, FEM converts the governing field equations into a system of algebraic equations that can be solved incrementally. It provides a robust numerical framework for solving the coupled equilibrium and constitutive equations governing deformation at the grain scale. Building on this foundation, the present study adopts a fully integrated crystal plasticity finite element workflow organized into three main stages: pre-processing, finite element solution, and post-processing. Representative polycrystalline aggregates were generated and also meshed using the open-source tessellation software Neper, where grain morphology and crystallographic orientations were defined based on the specific microstructural cases investigated in this thesis. Then, these models were then imported into Abaqus/Standard.

The constitutive behavior of each grain was introduced through a user-material subroutine (UMAT). The formulation implemented in this work is primarily based on the classical single-crystal plasticity model developed by Huang [2], a widely referenced framework in CPFEM studies. Nevertheless, several numerical components were adapted from the Oxford UMAT implementation by Demir et al. [15].

Throughout the simulations, Abaqus functioned not only as the computational engine for solving the constitutive updates but also as the environment for extracting post-processed data, including stress–strain responses, slip activity maps, grain-level strain distributions, and orientation-dependent deformation patterns.

4.1.1 Forward Gradient Time Integration Scheme

The constitutive updates within the UMAT rely on a forward-gradient (θ -method) time integration scheme. This approach follows the tangent modulus formulation of Peirce, Shih, and Needleman [25], originally developed to capture viscoplastic slip kinetics in crystalline materials. Within a time increment Δt , the shear strain increment $\gamma^{(\alpha)}$ on slip system α is defined as follows:

$$\Delta\gamma^{(\alpha)} = \gamma^{(\alpha)}(t + \Delta t) - \gamma^{(\alpha)}(t)$$

with linear interpolation:

$$\Delta\gamma^{(\alpha)} = \Delta t \left[(1 - \theta) \dot{\gamma}_t^{(\alpha)} + \theta \dot{\gamma}_{t+\Delta t}^{(\alpha)} \right]$$

Here $\dot{\gamma}_t^{(\alpha)}$ describes evaluated slipping rate at time t . θ represents Euler time integration scheme. Slip activity $\dot{\gamma}^{(\alpha)}$ on a system α can be modeled as a function of the applied shear stress $\tau^{(\alpha)}$ and the present strength $g^{(\alpha)}$. Thus:

$$\dot{\gamma}_{t+\Delta t}^{(\alpha)} = \dot{\gamma}_t^{(\alpha)} + \frac{\partial \dot{\gamma}^{(\alpha)}}{\partial \tau^{(\alpha)}} \Delta\tau^{(\alpha)} + \frac{\partial \dot{\gamma}^{(\alpha)}}{\partial g^{(\alpha)}} \Delta g^{(\alpha)}$$

Hence, the increments of shear strain, $\Delta\gamma^{(\alpha)}$, can be obtained as follows:

$$\Delta\gamma^{(\alpha)} = \Delta t \left[\dot{\gamma}_t^{(\alpha)} + \theta \frac{\partial \dot{\gamma}^{(\alpha)}}{\partial \tau^{(\alpha)}} \Delta\tau^{(\alpha)} + \theta \frac{\partial \dot{\gamma}^{(\alpha)}}{\partial g^{(\alpha)}} \Delta g^{(\alpha)} \right] \quad (4.1.1.1)$$

4.1.2 Incremental Formulation

This section establishes the formulations for the increments of shear strain $\Delta\gamma^{(\alpha)}$, resolved shear stress $\Delta\tau^{(\alpha)}$, and the instantaneous strength $\Delta g^{(\alpha)}$ across all slip systems, expressed as functions of the strain increments $\Delta\varepsilon_{ij}$, and the time increment Δt . To obtain current strength in terms of shear strain and dislocation density increments, following equation is used:

$$\Delta g^{(\alpha)} = h_{\alpha\beta} \text{sign}(\dot{\gamma}_t) \Delta\gamma^{\beta} + \frac{Gb^{(\alpha)}\xi}{2\sqrt{\rho_{tot}}} \Delta\rho_{tot} \quad (4.1.2.1)$$

The change in resolved shear stress $\Delta\tau^{(\alpha)}$ is determined by the total strain increment $\Delta\varepsilon_{ij}$, considering the elastic law defined by Hill and Rice [18], and it can be split of strain into plastic and lattice contributions.

$$\Delta\tau^{(\alpha)} = \left[\mathbb{C}_{ijkl} P_{kl}^{(\alpha)} + W_{ik}^{(\alpha)} \tau_{jk} + W_{jk}^{(\alpha)} \sigma_{ik} \right] \left[\Delta\varepsilon_{ij} - \sum_{\beta} P_{ij}^{(\beta)} \Delta\gamma^{(\beta)} \right] \quad (4.1.2.2)$$

Once the total strain increment $\Delta\varepsilon_{ij}$ is determined, the values of $\Delta\gamma^{(\alpha)}$ are obtained by solving a linear algebraic equation constructed from the (4.1.2.1) and (4.1.2.2) into (4.1.1.1) as follows:

$$\begin{aligned} & \sum_{\beta} \left\{ \delta_{\alpha\beta} + \theta \Delta t \frac{\partial \dot{\gamma}^{(\alpha)}}{\partial \tau^{(\alpha)}} \left[\mathbb{C}_{ijkl} P_{kl}^{(\alpha)} + W_{ik}^{(\alpha)} \tau_{jk} + W_{jk}^{(\alpha)} \tau_{ik} \right] P_{ij}^{(\beta)} \right. \\ & \quad \left. - \theta \Delta t \frac{\partial \dot{\gamma}^{(\alpha)}}{\partial g^{(\alpha)}} h_{\alpha\beta} \text{sign}(\dot{\gamma}_t^{(\beta)}) \right\} \Delta\gamma^{(\beta)} \\ & = \dot{\gamma}_t^{(\alpha)} \Delta t + \theta \Delta t \frac{\partial \dot{\gamma}^{(\alpha)}}{\partial \tau^{(\alpha)}} \left[\mathbb{C}_{ijkl} P_{kl}^{\alpha} + W_{ik}^{(\alpha)} \tau_{jk} + W_{jk}^{(\alpha)} \tau_{ik} \right] \Delta\varepsilon_{ij} \\ & \quad + \theta \Delta t \left(\frac{\partial \dot{\gamma}^{(\alpha)}}{\partial g^{(\alpha)}} \right) \frac{Gb^{(\alpha)}\xi}{2\sqrt{\rho_{tot}}} \Delta\rho_{tot} \end{aligned}$$

where $\delta_{\alpha\beta}$ denotes the Kronecker delta. After obtaining $\Delta\gamma^{(\alpha)}$ as functions of the strain increment $\Delta\varepsilon_{ij}$, and $\Delta\rho_{tot}$ the remaining incremental variables can be

computed by applying the relevant relations. The forward gradient formulation leads to a linear system, where the left-hand side consists of the coefficient matrix \mathbf{A} , and the right-hand side represents the known slip vector \mathbf{p} .

$$[\mathbf{A}]\{\Delta\gamma\} = \{\mathbf{p}\}$$

As a result, the slip increments can be compactly expressed as:

$$\{\Delta\gamma\} = [\mathbf{A}]^{-1}\{\mathbf{p}\}$$

After computing the slip increments, the plastic velocity gradient is obtained by applying:

$$\mathbf{L}^P = \sum_{\alpha} \frac{\Delta\gamma^{(\alpha)}}{\Delta t} \mathbf{s}^{*(\alpha)} \otimes \mathbf{m}^{*(\alpha)}$$

Then the plastic part of the deformation gradient can be calculated as:

$$\mathbf{F}^P = (\mathbf{I} - \mathbf{L}^P \Delta t)^{-1} (\mathbf{F}^P)_t$$

Crystal orientation matrix updates are performed using incremental rotations which are obtained from the elastic spin tensor increment according to:

$$\mathbf{K}^T = \mathbf{K}_t^T + \Delta\Omega^* \mathbf{K}_t^T$$

In this study, a finite element (FE) framework was established to replicate the mechanical behavior of a polycrystalline copper specimen under simple compression loading, aiming to investigate the role of grain boundaries on plastic deformation. The modeling procedure followed a systematic workflow involving polycrystal generation, meshing, material model implementation through a user subroutine (UMAT), and detailed convergence analyses.

4.2 Polycrystal Generation

Representative polycrystalline geometries were constructed using Neper v4.5.2. The computational domain was defined as a cylindrical representative volume element (RVE) with a 1:1 height-to-diameter ratio. In Fig. 4.2-1 one example of created RVE by Neper is presented. To investigate the influence of model scale on numerical resolution and to identify the size at which the results converge, three different RVE dimensions were generated with diameters of 1 mm, 10 mm, and 100 mm. Each RVE was independently tessellated using three-dimensional Voronoi construction to ensure consistent grain morphology across scales. This systematic variation in RVE size enabled the assessment of convergence behavior in terms of both stress–strain response and intergranular deformation characteristics.



Figure 4.2-1 RVE created by Neper to be used in CPFEM simulation

Four distinct microstructures were generated containing 1, 10, 100, and 500 grains to systematically examine the influence of microstructural refinement. The corresponding average grain diameters were approximately 1817, 843, 391, 229 μm , respectively, while the grain aspect ratio (AR) was maintained within 1.0 ± 0.1 to prevent artificial anisotropy. All polycrystals were constructed using 3D Voronoi

tessellation, ensuring isotropic grain morphology and statistically representative topologies.

Crystallographic orientations were defined for each grain using Bunge Euler angles (ϕ_1, Φ, ϕ_2) within the crystal plasticity framework. For each grain, all twelve $\{111\}$ $\langle 110 \rangle$ slip systems of the FCC crystal structure were evaluated, and the maximum Schmid factor among these systems was used as the primary indicator for slip system activity. To systematically represent orientation dispersion, multiple grain sets were generated around a selected reference Euler angle, each with different standard deviations in the orientation distribution. This controlled approach ensured that the model included grains with varying alignment relative to the loading axis, enabling consistent activation of multiple slip systems across the RVE. The defined orientations were directly coupled to the elastic stiffness tensor in the UMAT implementation, ensuring that the crystallographic variation of each grain was accurately represented in the finite element simulations.

4.3 Meshing and Convergence Study

The generated polycrystalline geometries were discretized using C3D10 quadratic tetrahedral elements, and it visualized in Fig. 4.3-1, which include four integration points per element. This element formulation was selected to capture the strain gradients and rotation fields within individual grains with sufficient accuracy, as these gradients directly influence the evolution of geometrically necessary dislocations (GNDs) in crystal plasticity analyses.

Mesh refinement was controlled through the Neper user defined dimensionless scaling factor which defines the characteristic element length, rcl , relative to the average grain size. Mesh length for each grain, cl , can be written as:

$$cl = \frac{rcl}{l_{cell}}$$

where l_{cell} is characteristic length of a grain. In Neper, the characteristic length of a cell is computed approximately as:

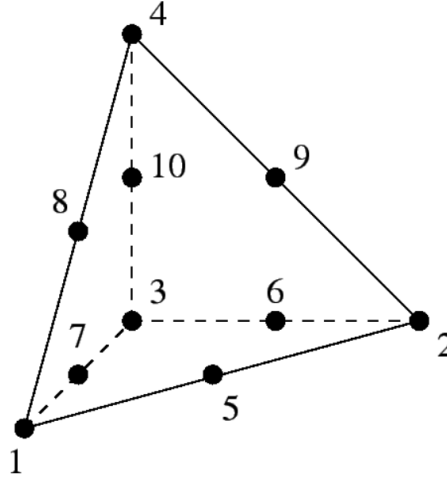


Figure 4.3-1 Schematic representation of C3D10 Meshing Element

$$l_{cell} = (V_{cell})^{\frac{1}{3}}$$

where V_{cell} is the cell volume. Multiple meshing levels were generated by systematically adjusting this parameter to evaluate the effect of spatial resolution on local deformation fields and numerical stability. The meshing procedure aimed to ensure that each grain was represented by an adequate number of elements to accurately capture intragranular slip and maintain smooth stress transfer across grain boundaries.

In selecting the mesh parameters, special attention was given to achieving a balance between numerical precision and computational efficiency. Excessive refinement can significantly increase the total number of elements and, consequently, the computation time, without providing meaningful improvement in local stress–strain predictions. Conversely, an overly coarse mesh may suppress strain gradients and underrepresent the anisotropic plastic response characteristic of FCC crystals. Therefore, a range of mesh densities was evaluated until the computed reaction forces, and global stiffness exhibited consistent behavior across successive

refinements. The finalized mesh configurations were subsequently imported into Abaqus/Standard for use with the implemented UMAT, forming the baseline discretization for all simulation cases.

4.4 Boundary Conditions and Loading

To replicate the kinematics of an experimental uniaxial compression test, reference points (RPs) were created to represent the top and bottom control surfaces of the cylindrical specimen. The nodes located on the upper and lower faces of the specimen were kinematically coupled to these reference points using coupling constraints, ensuring uniform displacement and rotation behavior across each surface. The bottom reference point was fully constrained in the axial (z) direction, while remaining free to expand in the radial (r) direction and rotate about the cylinder axis. This configuration allowed realistic lateral expansion of the specimen during compression while preventing rigid-body motion. The top reference point followed the same constraint logic, with an additional displacement-controlled loading corresponding to 20% compression applied along the z-axis to induce uniaxial compression. The constructed boundary conditions and loadings can be seen in the following Fig. 4.4-1 which is directly exported from the Abaqus.

These boundary conditions were designed to avoid constraint of lateral strain and to preserve overall mechanical equilibrium during deformation. The axial reaction force was extracted from the top reference point and subsequently used to calculate the macroscopic stress–strain response. Engineering quantities were later converted to true stress–true strain using logarithmic definitions, ensuring consistent comparison across all simulation cases. In addition to boundary constraints, the contact interaction between the specimen and the loading interfaces was defined through the same coupling-based framework. The interface behavior was assumed to be frictionless, allowing free radial expansion of the specimen without resistance. This assumption was intentionally made to eliminate barreling effects and to isolate

the intrinsic grain-scale plasticity mechanisms governed by grain orientation and boundary interactions. As the primary objective of this study was to analyze microstructural deformation behavior rather than macroscopic frictional influence, neglecting friction was considered.

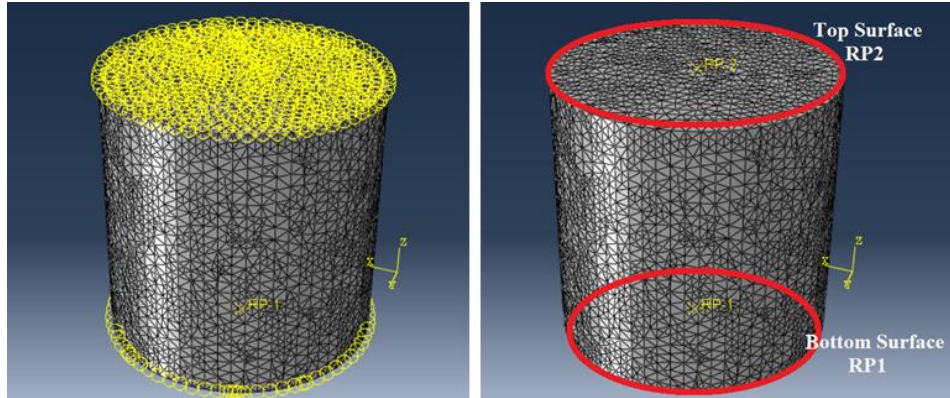


Figure 4.4-1 Boundary conditions and related Reference Points (RP) are represented.

4.5 Selected Material Information

The material parameters employed in this study are summarized in Table 4.4-1. All values were directly adopted from Demir, E. et al. [15]. This reference provides a validated parameter set specifically calibrated for FCC copper, ensuring consistency with the crystal plasticity constitutive framework used in the present work.

Table 4.5-1 Selected Material Parameters of Cu for CPFEM

Model Parameters	Value	Units
C_{11}	170	GPa
C_{12}	124	GPa
C_{44}	75	GPa
b	$2.56 \cdot (10^{-4})$	μm
g_0	16	MPa
h_0	250	MPa
n	2.5	
q	1.4	

The parameters include both elastic constants and crystal plasticity hardening coefficients, which collectively define the anisotropic elastic response and the evolution of slip resistance at the grain level. The elastic stiffness components describe the cubic elastic symmetry of copper, while the crystallographic slip parameters (such as n , and q) govern the rate-dependent viscoplastic behavior implemented in the UMAT formulation

CHAPTER 5

RESULT AND DISCUSSION

The results obtained from the developed crystal plasticity finite element model are presented and discussed in this chapter for pure compression of samples. Building upon the modeling framework defined in the previous section, the analyses here aim to verify the predictive capability of the model and to interpret the deformation mechanisms emerging from the polycrystalline microstructure. The results are structured to first isolate the numerical effects of mesh density and RVE size through preliminary convergence analyses. Subsequently, the study demonstrates how the intrinsic microstructural parameters, grain size, grain orientation, and their combined interactions govern the simulated mechanical response of copper under uniaxial compression.

The first part of the analysis focuses on the numerical consistency of the model, where both mesh density and RVE size effects were examined to confirm convergence and eliminate size-dependent artifacts. By systematically adjusting the element characteristic length (rcl) and the RVE dimensions, the minimum computational resolution required to capture stable stress–strain behavior and accurate intergranular stress gradients was identified.

Once the numerical stability of the model was established, attention was shifted toward understanding the microstructural origins of plastic deformation. The analyses explored how grain orientation, grain size, and their mutual interactions affect the macroscopic hardening response and microscopic strain localization. Single-crystal simulations were used to isolate the role of crystallographic alignment, while polycrystalline aggregates enabled examination of collective deformation behavior across grains with controlled orientation dispersions. Similarly, models containing varying numbers of grains, from coarse-grained to fine-grained

structures, were analyzed to assess the influence of grain refinement on stress distribution and slip system activity.

The results presented in the following sections reveal how geometric scale, microstructural configuration, and crystallographic texture interact to shape the overall deformation response. This comprehensive evaluation not only validates the robustness of the developed CPFEM framework but also provides a mechanistic understanding of how grain structure and orientation coupling governs the plastic behavior of polycrystalline copper.

5.1 Model Convergence – Sensitivity Analysis

5.1.1 Mesh Density

Mesh sensitivity was first evaluated using a single-grain specimen by varying the previously introduced Neper rcl parameter between 0.6 and 0.1, which directly controls the characteristic element length in the generated mesh. Each configuration was meshed using C3D10 quadratic tetrahedral elements. The selected rcl range reflects a balance between computational efficiency and accuracy in capturing crystal-scale fields. Coarser meshes corresponding to $rcl \approx 0.6$ provide faster simulations and allow rapid screening of boundary-condition effects; however, they may insufficiently resolve the steep deformation gradients typical of crystal plasticity. Conversely, progressively smaller values approaching $rcl = 0.1$ substantially improve spatial resolution and the fidelity of slip localization patterns, but at a significantly increased computational cost. Evaluating meshes within this 0.6–0.1 interval therefore enables identification of a mesh density that is fine enough to capture the essential intragranular mechanisms such as lattice rotation, slip accumulation, and heterogeneity of the stress field, while avoiding unnecessary refinement that would result in prohibitive computational expense. In following Fig. 5.1-1, the selected mesh sizes are visualized from 0.1 to 0.6.

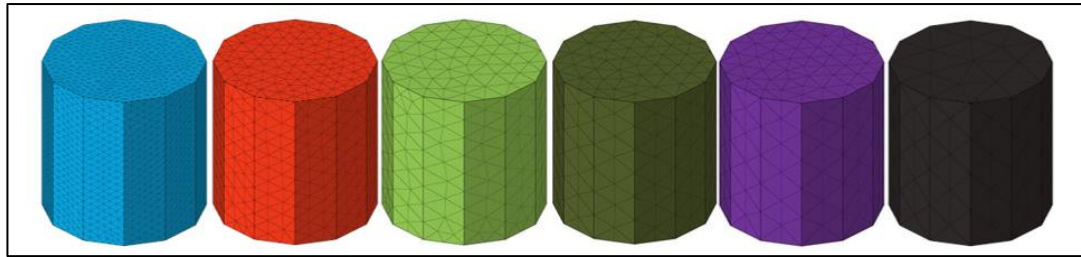


Figure 5.1-1 RVE models with 6 different mesh density – rcl 0.1 to 0.6.

Convergence was determined based solely on the overlap of the true stress–true strain curves obtained from successive mesh refinements. Figure 5.1-2 presents the true stress–true strain responses obtained from the single-grain simulations performed with varying mesh resolutions, defined by rcl values ranging from 0.6 to 0.1. To better illustrate the residual deviation between the curves, a zoomed-in view of the 20% strain region is included in the lower-right corner of the figure. This inset highlights the small yet measurable differences between mesh densities and visually confirms the convergence behavior discussed above.

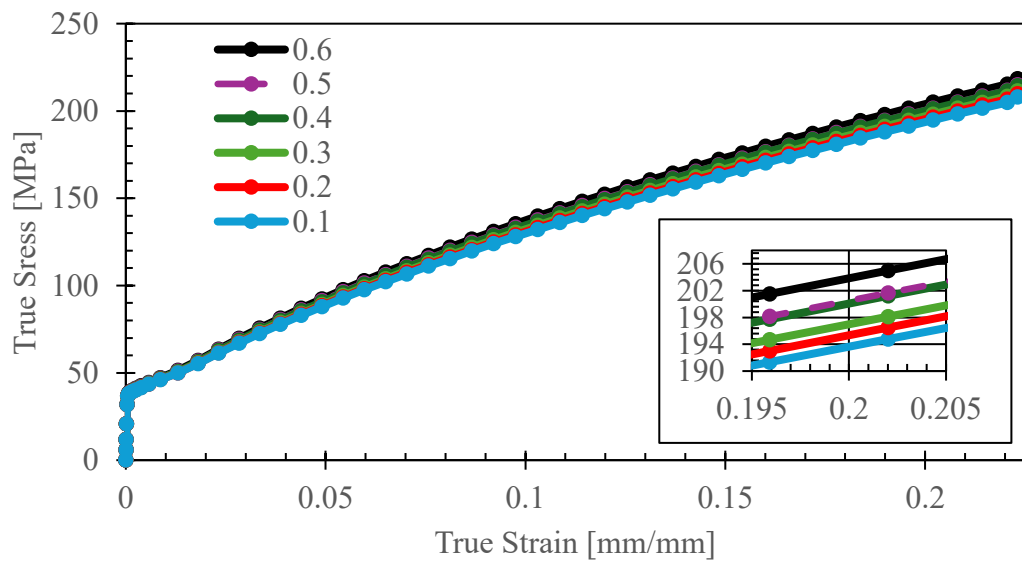


Figure 5.1-2 True stress true strain curves for 6 different mesh element sizes

Table 5.1-1 quantitatively summarizes the mesh convergence behavior presented in Figure 5.1-2 by listing the total number of elements and corresponding true stress

values at 20 % strain for each rcl configuration. As the element size decreases, the model response gradually stabilizes between $rcl = 0.6$ and $rcl = 0.2$, the true stress decreases by approximately 4.15%. However, further refinement to $rcl = 0.1$ results in less than 0.9% additional change, while increasing the total element count and computation time by nearly an order of magnitude. In principle, the finest mesh generated with the smallest rcl value provides the most accurate results due to resolving sharp slip gradients, lattice curvature, and stress heterogeneity more faithfully. However, based on the trade-off between accuracy and computational efficiency, $rcl = 0.2$ was selected as the reference mesh resolution for all subsequent single- and polycrystalline simulations.

Table 5.1-1 True Stress Comparison at 0.2 Strain for Meshing Parameters

Total Elements	RCL Size	True Stress at 0.2 Strain [MPa]
607	0.6	205.00
1009	0.5	201.60
1134	0.4	201.20
3047	0.3	198.12
13945	0.2	196.50
127892	0.1	194.78

5.1.2 RVE Size

Using the converged mesh resolution as $rcl = 0.2$, the influence of RVE size was examined for cylindrical single-crystal domains with diameters of 0.1, 1, and 10 mm. Each domain maintains a height-to-diameter ratio of unity. The boundary and loading conditions were identical for all configurations, with displacement-controlled compression applied through reference-point couplings. The geometrical representations, 0.1 mm (blue), 1 mm (red), and 10 mm (green), of these single-

crystal RVEs are illustrated in Figure 5.1-3. The 0.1 mm model is highlighted in a box, with its enlarged view shown on the right for clarity.

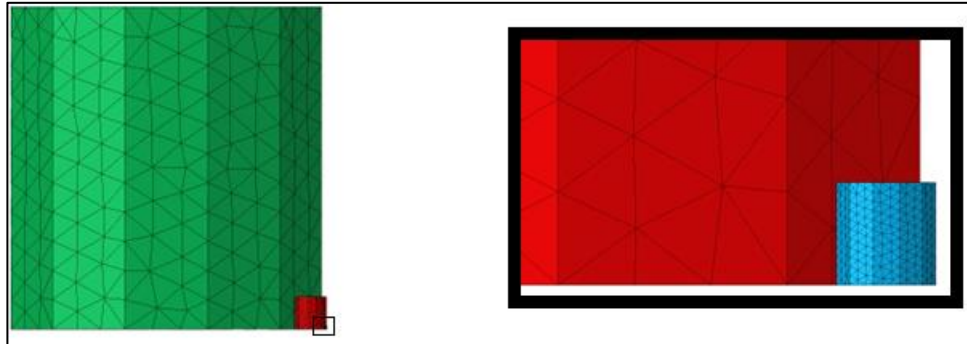


Figure 5.1-3 Different RVE Sizes schematic view of 0.1 mm (blue), 1 mm (red), and 10 mm (green). The 0.1 mm model is highlighted in a box.

As shown in Figure 5.1-4, the 0.1 mm RVE exhibited a true stress of approximately 196 MPa at 20 % strain, whereas both the 1 mm and 10 mm models reached around 185 MPa. This higher stress level in the smallest specimen originates from the stronger boundary constraint inherent to smaller volumes, where the proportion of constrained surface nodes relative to the free interior is considerably larger. As a result, lateral expansion is more restricted, producing a slightly elevated triaxial stress state. With increasing specimen size, the influence of this constraint diminishes, and the stress–strain response converges toward a stable value. A magnified view of the 20% strain region is provided in the lower-right corner to emphasize the minor deviations between the curves and visually confirming the convergence trend. The nearly identical responses obtained for the 1 mm and 10 mm models confirm that the deformation behavior becomes size-independent after 1mm. Consequently, the 1 mm RVE was selected as the reference configuration for all subsequent polycrystalline analyses, providing a physically representative response while maintaining computational efficiency.

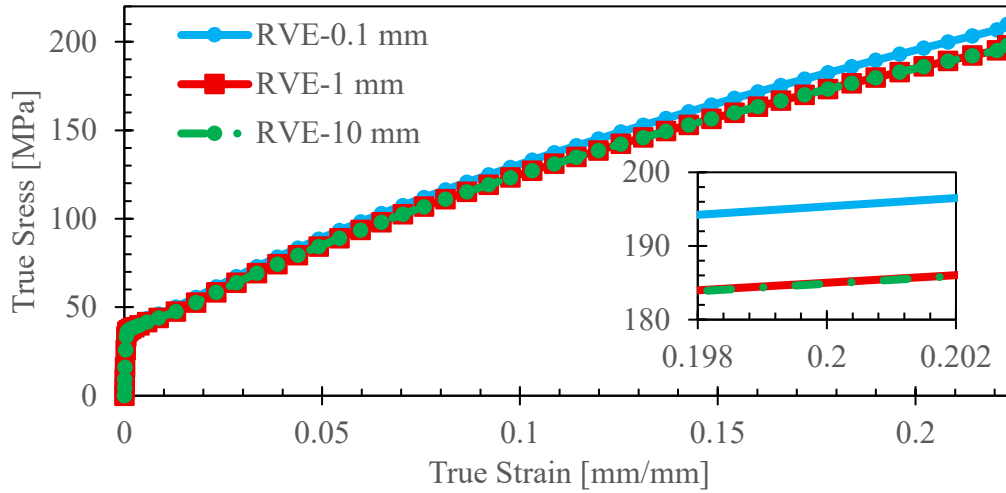


Figure 5.1-4 True stress & strain curve for different RVE Sizes schematic view of 0.1 mm (blue), 1 mm (red), and 10 mm (green). %20 strain region is highlighted in right – below corner.

5.2 Grain Size Effect

To examine the grain-size effect independently of texture, a single crystal RVE and polycrystalline RVEs containing 10, 100, and 500 grains were generated and analyzed under identical boundary and loading conditions. Each model was created using Neper in its default tessellation mode and they can be seen in below Fig. 5.2-1. In this process, Neper randomly places a set of seed points inside the cylindrical domain and constructs a 3D Voronoi tessellation around them. Each seed represents the center of a grain, and the random placement ensures that no spatial bias or preferred texture is introduced. Because the seed positions are determined by a random number generator, every realization produces a unique grain arrangement while maintaining overall statistical uniformity. This approach guarantees that the resulting microstructures are truly random in grain size, shape, and position, providing a reliable basis for evaluating the influence of grain size on the mechanical response.

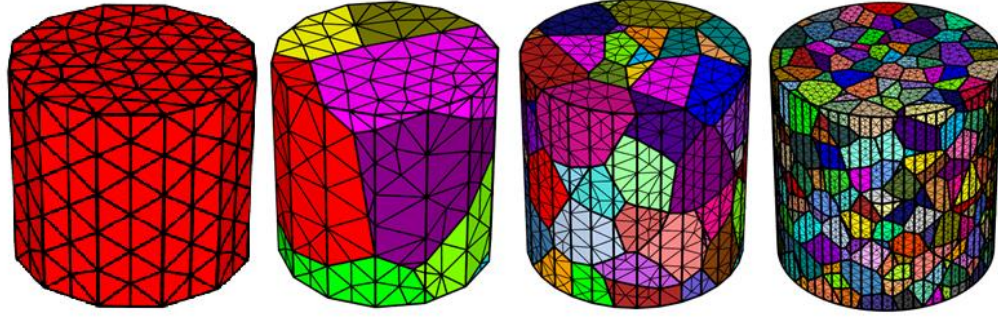


Figure 5.2-1 RVE models for a single crystal and polycrystals with 10, 100, 500 grains respectively

Orientations for these randomly created grains were assigned by Neper in a way that no preferred texture component dominates the macroscopic response. Mesh settings and boundary/loading definitions were kept identical to the convergence baseline to ensure that any systematic change in response originates from grain size, not from numerical parameters.

Table 5.2-1 reports, for each RVE, the grain count N , the cylinder volume, and the average grain size. For a cylindrical of volume V partitioned into N grains, the average grain volume is:

$$\bar{V}_g = \frac{V}{N}$$

Each grain is assumed as a spherical shape and consecutively an average grain diameter can be calculated as follows:

$$d_{eq} = \left(\frac{6}{\pi} \bar{V}_g \right)^{\frac{1}{3}}$$

The overall true stress–true strain responses for the random polycrystalline RVEs with 1, 10, 100, and 500 grains are presented in Figure 5.2-2. A consistent grain-size strengthening trend is observed for constant RVE volume. As the number of grains increases and the average grain size decreases, the macroscopic flow stress rises. The

single-grain model exhibits the lowest stress level throughout deformation, while the 100 and 500 grain configurations display significantly higher stress during plasticity.

Table 5.2-1 Average Grain Size & Number of Grain Correlations

The cylinder RVE volume is 3.142 [mm]³.

Number of Grains	Average Grain Volume [mm] ³	Average Grain Diameter [μm]
1	3.142	1817
10	0.314	843
100	0.031	391
500	0.006	229

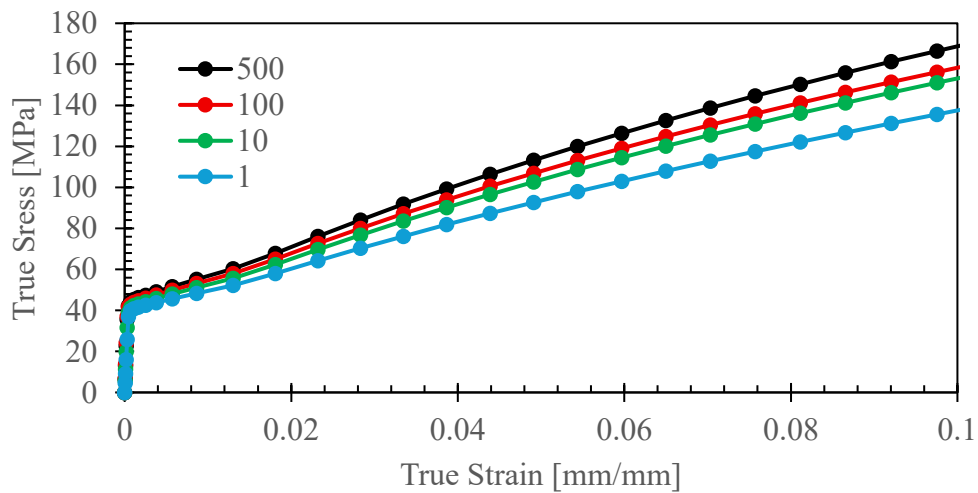


Figure 5.2-2 True stress-strain curves for different grain numbers in RVE.

In following Fig. 5.2-3, particularly the 0.05–0.1 true strain region is highlighted to clearly illustrate how decreasing grain size leads to higher flow stresses and more distinct divergence between the single, 10, 100, and 500-grain polycrystalline configurations. The flow stress determination procedure is illustrated in Fig. 5.2-4, where each curve is magnified for clarity. A linear reference line (shown in purple) was extended from the initial slope of each curve and translated to intersect the strain

axis at 0.002, following the conventional 0.2% offset method. The intersection points between these offset lines and the corresponding stress–strain curves define the yield stress for each grain configuration. This approach allows consistent comparison across microstructures with different stiffness or nonlinearity near yield, ensuring that the identified yield points reflect true plastic initiation.

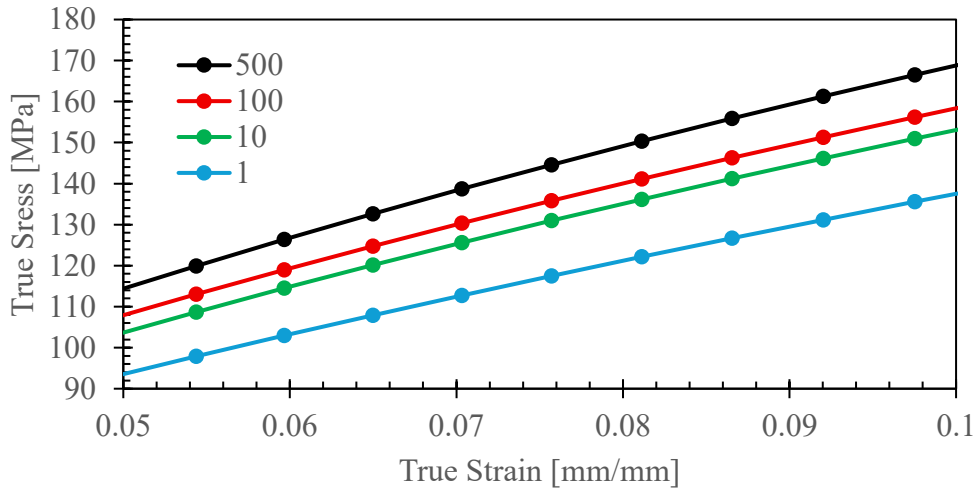


Figure 5.2-3 Highlighted True stress-strain curves for different grain numbers in RVE.

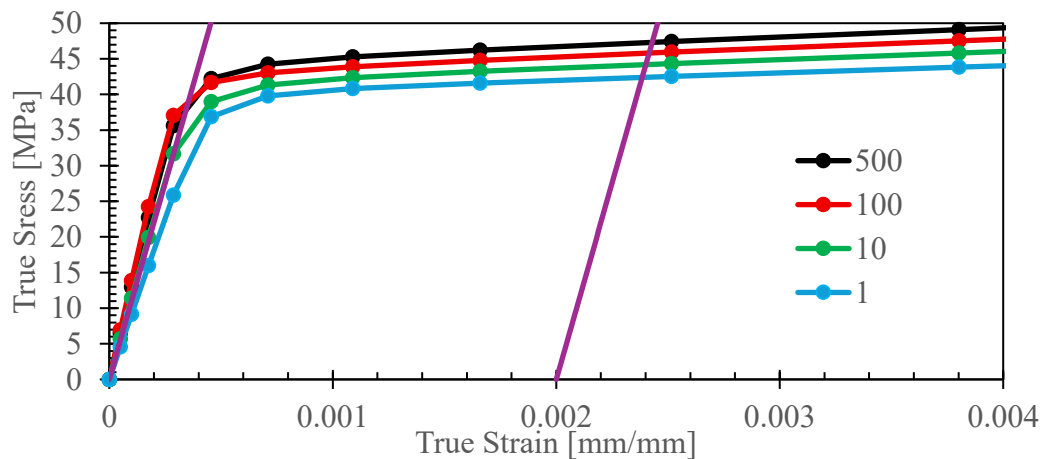


Figure 5.2-4 Closer look to the 0.2% strain for different number of grains.

The resulting flow stresses and stress levels at 10% strain are summarized in Table 5.2-2. As the average grain size decreases from 1817 μm (1 grain) to 229 μm (500 grains), the yield stress increases from 41.86 MPa to 47.25 MPa, while the stress at 10% strain rises from 125.0 MPa to 168.8 MPa. The strengthening effect between the coarsest and finest microstructures corresponds to an increase of approximately 13% in flow stress and 35% in macroscopic strength. These results confirm the classical grain-size strengthening behavior, where the higher grain-boundary density and increased geometrically necessary dislocation (GND) accumulation in smaller grains inhibit slip transmission, resulting in elevated overall strength [29].

Table 5.2-2 The resulting flow stresses and stress levels at 10% strain for different grain size

Grain Number	Av. Grain Size [micrometer]	Flow Stress [MPa]	Stress at 0.1 Strain [MPa]
500	229	47.25	168.79
100	391	45.52	158.37
10	843	44.06	153.04
1	1817	41.86	125.00

To validate the grain-size dependence of the simulated flow stress, the results were fitted to the classical Hall–Petch relation:

$$\sigma_y = \sigma_0 + k_y d^{-1/2}$$

where k_y is Hall Petch constant, σ_y is yield strength, σ_0 is lattice friction. The corresponding plot of flow stress versus $d^{-1/2}$ exhibited a good linear correlation ($R^2 \approx 0.97$), confirming that the simulated data follow Hall–Petch scaling. The fitted parameters were $\sigma_0 = 39.40$ [MPa] and $k_y = 120.79$ [MPa] $\cdot \mu\text{m}^{\frac{1}{2}}$ and the related curves can be seen in following Figure 5.2-5.

Results show good agreement with the experimentally reported values for pure copper presented by Cordero et al., who reported $\sigma_0 \approx 40$ MPa and $k_y \approx$

110MPa· $\mu\text{m}^{1/2}$ [29]. The close correspondence between the simulated and experimental parameters validates the physical accuracy of the present CPFEM framework and confirms that the simulated grain-size strengthening behavior accurately reproduces the experimentally observed Hall–Petch scaling for copper. This agreement reinforces the reliability of the implemented constitutive formulation and supports the use of the current model for predictive studies of grain-size-dependent plasticity in FCC metals.

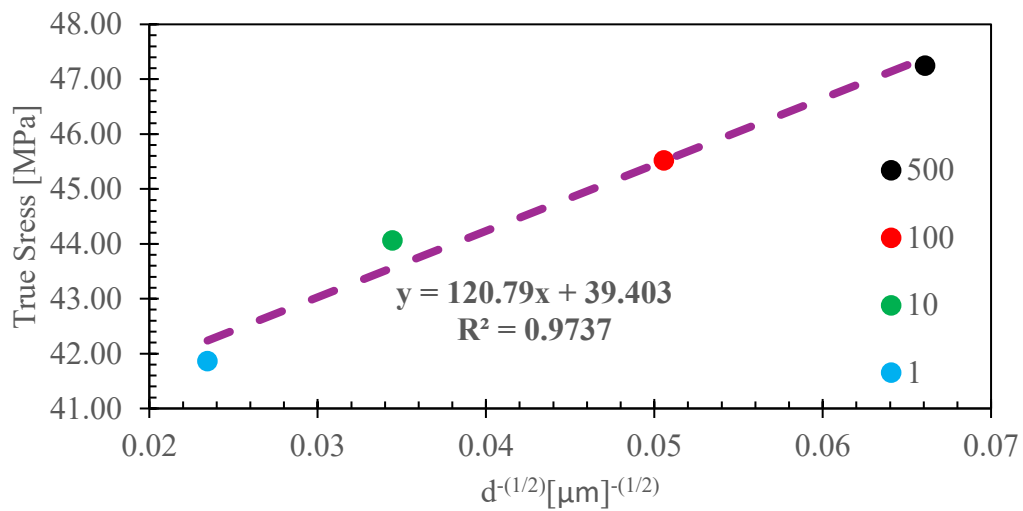


Figure 5.2-5 Hall-Petch plot with curve fitting for $\sigma_y = \sigma_0 + k_y d^{-1/2}$

5.3 Grain Orientation Effect

The influence of crystallographic orientation was examined by selecting a set of representative orientations that span different levels of slip. To construct this orientation set in a systematic way, the Schmid factor was used as an initial geometrical guide. Rather than serving as a predictive measure of strength, the Schmid factor here functioned solely as a selection criterion that quantified the alignment between the global loading axis and the primary $\{111\}\langle 110\rangle$ slip systems. The Schmid factor can take values between zero and 0.5, depending on the relative

angle between the loading axis, the slip plane normal, and the slip direction. As the Schmid factor approaches 0.5, a larger portion of the applied axial stress is resolved as shear on that slip system, and slip is more likely to occur on that system in the initial undeformed configuration. However, this condition holds only at the beginning of loading; once deformation starts, lattice rotation changes the geometric relations between the crystal axes and the loading direction, and the Schmid factors evolve during the simulation. After the orientations were defined, the actual mechanical response was controlled by the constitutive relations implemented in the UMAT, while the Schmid factor served only as the geometric reference for interpreting the influence of crystallographic alignment.

5.3.1 Single Crystal

In this section, a set of single-crystal orientations was generated by considering the initial Schmid factor distribution of the $\{111\}\langle 110 \rangle$ slip systems. For each selected orientation, the samples were then compressed up to 20% displacement to examine how crystallographic alignment influences the resulting stress–strain response and slip activity. The first Euler angle selected for this analysis was $(0^\circ, 45^\circ, 45^\circ)$. This was followed by the Euler angle of $(324^\circ, 108^\circ, 98^\circ)$, which produces a maximum Schmid factor close to 0.5. Finally, the effect of gradually increasing rotation was examined by varying the second Euler angle from 45° to 75° in increments of 5° in $(0^\circ, 45^\circ, 45^\circ)$ system.

5.3.1.1 Orientation with Euler Angle $(0^\circ, 45^\circ, 45^\circ)$

For the orientation defined by the Euler angle of $(0^\circ, 45^\circ, 45^\circ)$, the resulting Schmid factor distribution revealed a balanced but non-uniform activation of the primary $\{111\}\langle 110 \rangle$ slip systems, as summarized in Table 5.3-1. Specifically slip systems 4, 6, 7, and 8 exhibited the highest Schmid factors between 0.29 and 0.35. Two additional systems, 2 and 3, attained lower values of approximately 0.14, while the

remaining systems displayed factors predominantly below 0.10, indicating limited contribution to deformation. The maximum Schmid factor for this orientation, 0.35, was taken as the representative value characterizing its overall degree of alignment. This Schmid factor level corresponds to a partially resolved shear stress-efficient slip configuration compared to the Schmid factor of 0.5, making it an appropriate reference case for examining how crystallographic orientation influences the constitutive response under uniaxial compression.

Table 5.3-1 Schmid factors for single crystal with Euler angles of (0°, 45°, 45°)

Slip System	Slip Plane Normal	Slip Direction	Schmid Factor
1	(1,1,1)	[1, -1,0]	0.00
2	(1,1,1)	[0,1, -1]	0.14
3	(1,1,1)	[1,0, -1]	0.14
4	(-1,1,1)	[1,1,0]	0.29
5	(-1,1,1)	[0,1, -1]	0.06
6	(-1,1,1)	[1,0,1]	0.35
7	(1, -1,1)	[1,1,0]	0.29
8	(1, -1,1)	[0,1,1]	0.35
9	(1, -1,1)	[1,0, -1]	0.06
10	(1,1, -1)	[1, -1,0]	0.00
11	(1,1, -1)	[0,1,1]	0.14
12	(1,1, -1)	[1,0,1]	0.14

The total slip, γ , extracted from the CPFEM output is plotted for all twelve FCC slip systems under uniaxial compression. In agreement with the Schmid factor distribution in Table 5.3.1-1, slip activity is predominantly concentrated in systems 4, 6, 7, and 8, which exhibit the highest geometric alignment between respective slip direction and the loading axis. Systems 2, 3, 11, and 12 show moderate activation, whereas the remaining systems remain largely inactive throughout deformation. This non-uniform partitioning of slip among the systems reflects the partially aligned slip character of the Euler angle of (0°, 45°, 45°) orientation. Therefore, it produces a plastic response governed by several actively competing slip systems rather than a

single dominant mechanism. Figure 5.3-1 illustrates this behavior by presenting the accumulated slip (γ) contours for all twelve $\{111\}\langle 110\rangle$ slip systems for the Euler angle of $(0^\circ, 45^\circ, 45^\circ)$ orientation. More intense slip activity can be observable in systems (d), (f), (g), and (h), while the remaining systems contribute only marginally.

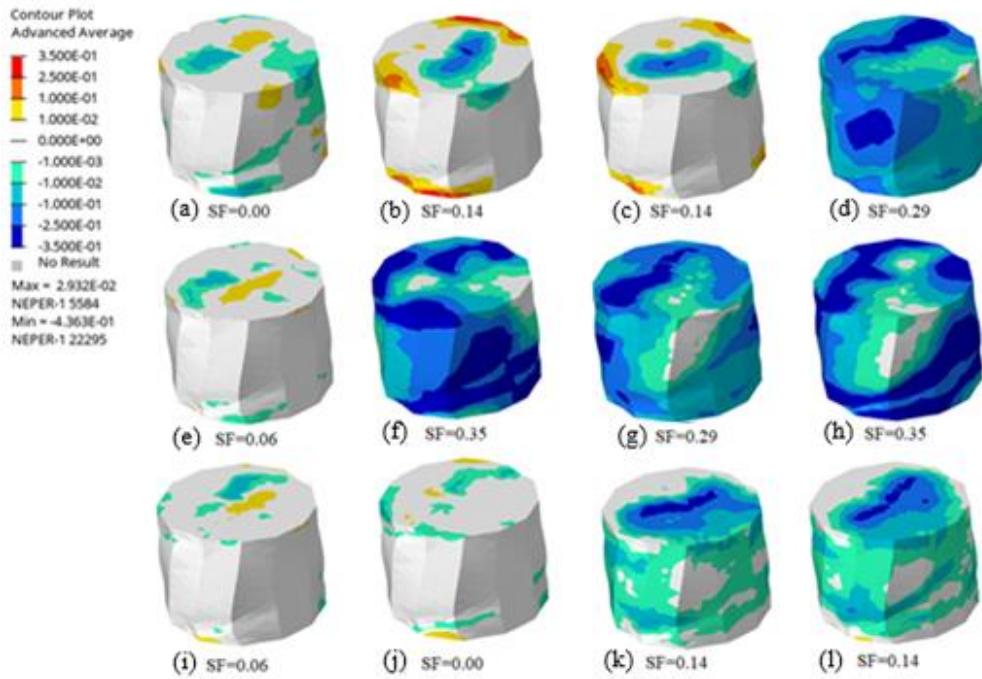


Figure 5.3-1 Total accumulated slip (γ) contours for all twelve $\{111\}\langle 110\rangle$ slip systems, (a) to (l), for the Euler angle of $(0^\circ, 45^\circ, 45^\circ)$

The true stress–true strain response for the $(0^\circ, 45^\circ, 45^\circ)$ orientation is shown in Figure 5.3-2, reaching a true stress of approximately 260 MPa at 20% strain under uniaxial compression, where the curve was obtained by applying 20% axial displacement to a reference point tied to the top surface and converting the resulting reaction force into true stress and true strain using the specimen cross-sectional area.

5.3.1.2 Orientation with Euler Angle of $(324^\circ, 108^\circ, 98^\circ)$

To identify the orientation expected to exhibit the lowest yield stress and smallest flow stress levels, the Euler angles were selected such that the maximum Schmid

factor among the twelve slip systems approached 0.5. This condition was satisfied for the orientation $(324^\circ, 108^\circ, 98^\circ)$, where slip system 10 reached a Schmid factor of 0.49, as summarized in Table 5.3-2. The overall Schmid factor distribution indicates that systems 4 and 10 shows higher Schmid factor values amongst other systems.

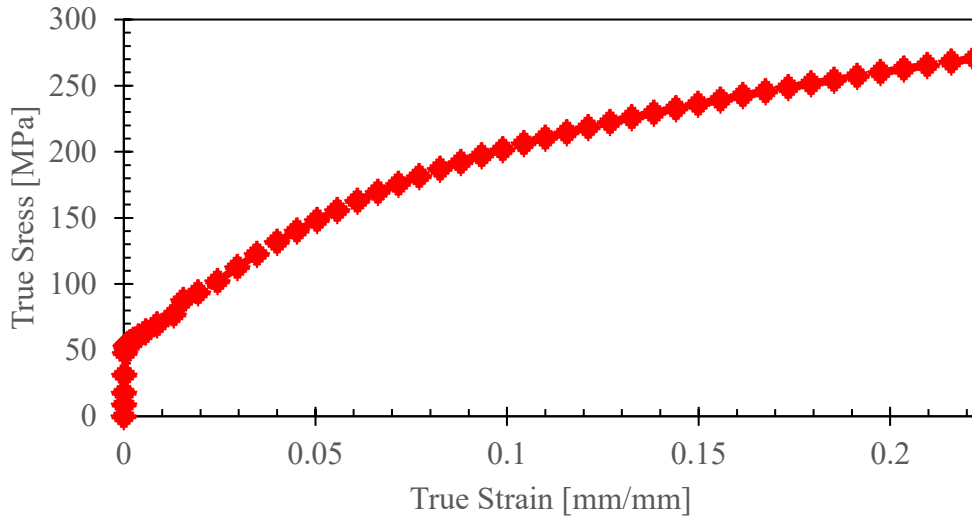


Figure 5.3-2 True stress-strain plot for $(0^\circ, 45^\circ, 45^\circ)$ single crystal

Table 5.3-2 Schmid factors for single crystal with Euler angles $(324^\circ, 108^\circ, 98^\circ)$

Slip System	Slip Plane Normal	Slip Direction	Schmid Factor
1	(1,1,1)	[1,-1,0]	0.22
2	(1,1,1)	[0,1,-1]	0.04
3	(1,1,1)	[1,0,-1]	0.26
4	(-1,1,1)	[1,1,0]	0.46
5	(-1,1,1)	[0,1,-1]	0.10
6	(-1,1,1)	[1,0,1]	0.36
7	(1,-1,1)	[1,1,0]	0.25
8	(1,-1,1)	[0,1,1]	0.14
9	(1,-1,1)	[1,0,-1]	0.39
10	(1,1,-1)	[1,-1,0]	0.49
11	(1,1,-1)	[0,1,1]	0.20
12	(1,1,-1)	[1,0,1]	0.29

The total accumulated slip contours for this orientation are shown in Figure 5.3-3 and indicate that slip activity is concentrated mainly in systems (d) and (j), which exhibit the most favorable geometric arrangement between the loading axis, the slip plane normal, and the slip direction. In these systems, the applied axial stress is resolved into a larger shear component on the active slip plane, causing them to accommodate most of the deformation. This behavior confirms that the $(324^\circ, 108^\circ, 98^\circ)$ orientation corresponds to the case with the lowest yield and flow stress levels among the simulated orientations.

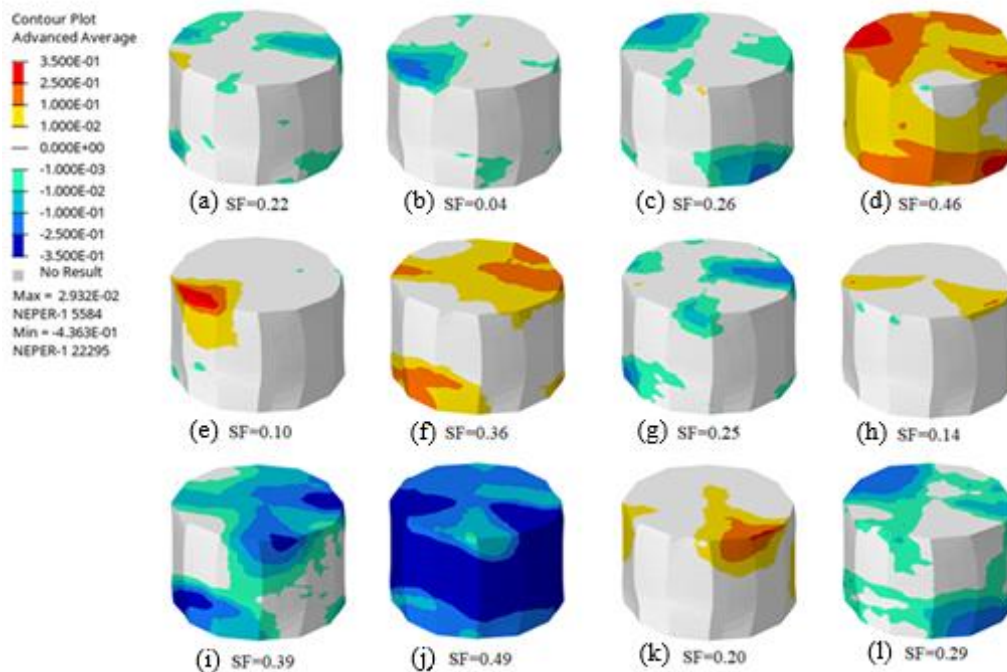


Figure 5.3-3 Total accumulated slip (γ) contours for all twelve $\{111\}\langle 110 \rangle$ slip systems, (a) to (l), for the Euler angle of $(324^\circ, 108^\circ, 98^\circ)$

The corresponding true stress–true strain curve is shown in Figure 5.3-4, plotted together with that of the $(0^\circ, 45^\circ, 45^\circ)$ orientation for comparison. The $(0^\circ, 45^\circ, 45^\circ)$ crystal, characterized by a maximum Schmid factor of 0.35, exhibits a higher flow of stress and a more pronounced hardening response. At 20 % strain, the $(324^\circ, 108^\circ, 98^\circ)$ orientation reaches a true stress of approximately 186 MPa, whereas the $(0^\circ,$

45°, 45°) case attains about 260 MPa, corresponding to a difference of roughly 39.7 % in plastic strength.

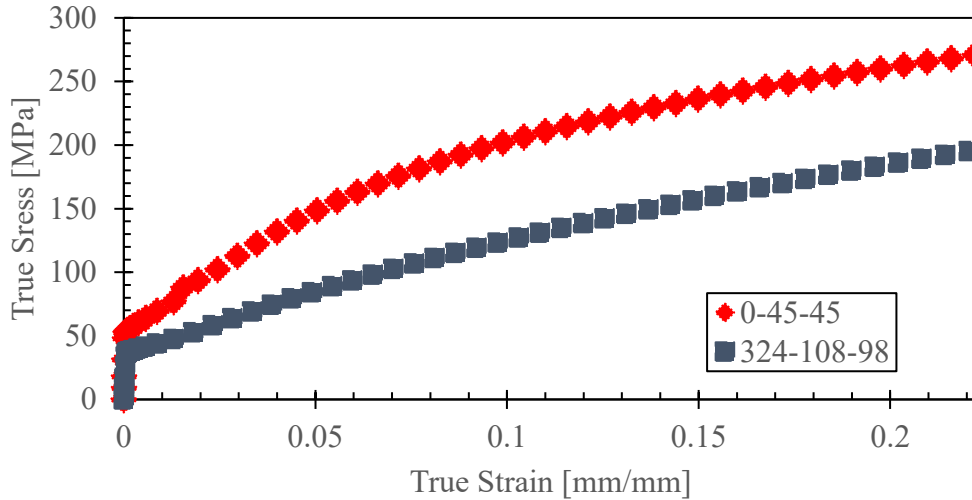


Figure 5.3-4 True stress-strain comparison plot for the Euler angles of (0°, 45°, 45°) and (324°, 108°, 98°) single crystals

5.3.1.3 Comparison of Different Orientations

To further examine the gradual influence of crystallographic alignment on the constitutive response, the crystal was incrementally rotated from (0°, 45°, 45°) to (0°, 75°, 45°) in 5° steps. The corresponding maximum Schmid factor and the true stress at 10% strain for each orientation are summarized in Table 5.3-3. The maximum Schmid factor increases from 0.28 at (0°, 55°, 45°) to 0.43 at (0°, 75°, 45°). Under the same critical resolved shear stress parameters defined in the constitutive model, a higher Schmid factor increases the portion of the applied force projected onto the slip systems, causing slip to initiate at lower macroscopic stress. Consistent with this mechanism, the true stress at 10% strain decreases from 243.56 MPa to 147.41 MPa, demonstrating a clear inverse relation between the initial geometric alignment of slip systems and the resulting flow strength.

The corresponding true stress–true strain curves for all orientations are shown in Figure 5.3-5. The curves exhibit a systematic reduction in both yield stress and hardening rate as the Schmid factor increases, confirming that orientations closer to slip configurations where a higher portion of the applied stress is resolved onto the slip systems deform more. The transition between the (0°, 55°, 45°) and (0°, 75°, 45°) orientations illustrates lower overall strength response, with a difference exceeding 95 MPa at 10% strain. This trend demonstrates that the macroscopic mechanical response is sensitive to crystallographic alignment, reflecting the direct dependence of slip activation on lattice orientation within the crystal plasticity framework for single crystal.

Table 5.3-3 Max Schmid Factors for single crystals with different Euler Bunge angles

Euler Angle	Max Schmid Factor	True Stress at %10 Strain [MPa]
0-55-45	0.28	243.56
0-50-45	0.31	226.92
0-60-45	0.33	209.96
0-45-45	0.35	202.66
0-65-45	0.37	179.56
0-70-45	0.41	158.43
0-75-45	0.43	147.41

To highlight the extremities of the orientation effect, the configurations with Euler angles of (0°, 55°, 45°) and (324°, 108°, 98°) were selected and presented in Fig. 5.3-6. The cases have highest and lowest yield stress and hardening rate amongst all others selected Euler angles, respectively. The Euler angle of (0°, 55°, 45°) exhibits a maximum Schmid factor of 0.28 and reaches a true stress of 243.56 MPa at 10% strain, whereas the Euler angle of (324°, 108°, 98°), with a Schmid factor of 0.49, reaches only about 155 MPa under the same loading conditions. Figure 5.3-7 presents the von Mises stress contours for the two single-crystal orientations. The

(324°, 108°, 98°) orientation exhibits lower overall stress levels, consistent with the activation of multiple slip systems, particularly the 10th slip, while the (0°, 55°, 45°) orientation shows more intense stress localization, reflecting its limited slip activity and higher resistance to plastic deformation.

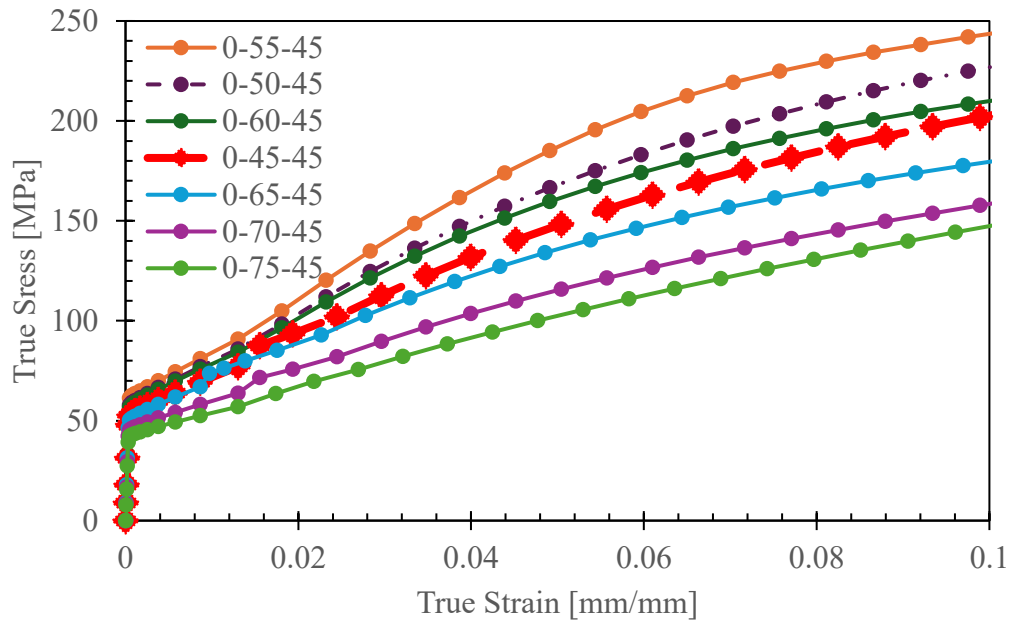


Figure 5.3-5 The corresponding true stress–true strain curves for all orientations

In summary, the single-grain analyses revealed a clear correlation between crystallographic orientation, slip system activation, and the resulting macroscopic behavior. As the loading direction produces a higher resolved shear stress on one or more $\{111\}\langle 110 \rangle$ slip systems, the macroscopic yield stress and flow strength become lower. Conversely, when the loading direction results in a lower resolved shear stress on the slip system, the transferred shear onto the available systems decreases, increasing the compressive force required to initiate slip and raising the macroscopic resistance. Moreover, the orientation direction was found to directly influence the hardening mechanism itself. Orientations such as Euler angle of (324°, 108°, 98°), which produce a higher resolved shear stress on one of the primaries $\{111\}\langle 110 \rangle$ slip systems (Schmid factor 0.49), exhibit nearly linear hardening because deformation is mainly carried by a limited set of slip systems with sustained

activity. In contrast, orientations such as Euler angle of $(0^\circ, 55^\circ, 45^\circ)$, which produce a lower resolved shear stress on the available slip systems (Schmid factor 0.28), display more nonlinear hardening due to the need for sequential activation of multiple systems as deformation progresses.

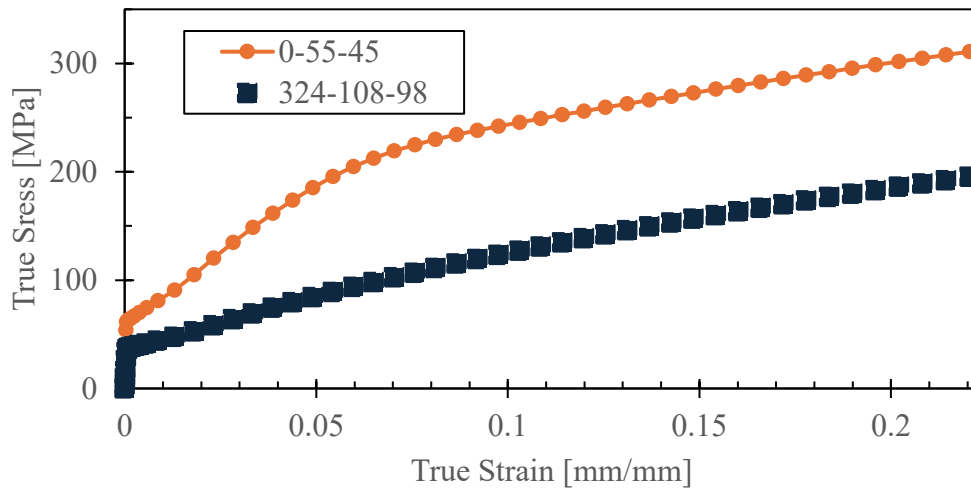


Figure 5.3-6 Two selected orientations true stress-strain curves for single crystals for lowest and highest true stresses

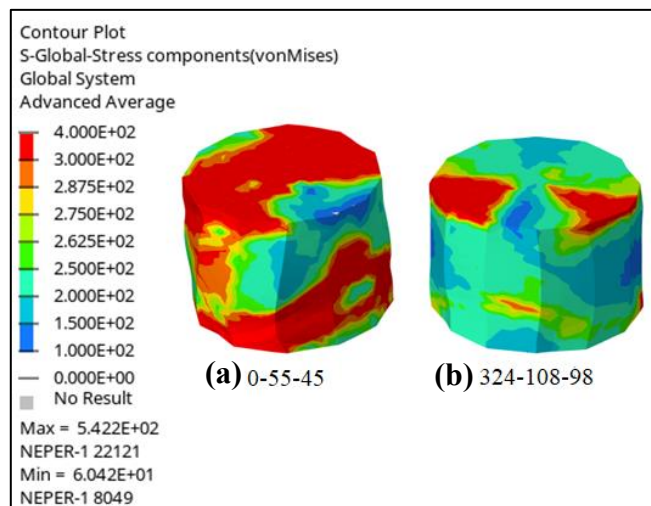


Figure 5.3-7 Presents the von Mises stress contours for the $(0^\circ, 55^\circ, 45^\circ)$ and $(324^\circ, 108^\circ, 98^\circ)$

5.3.2 Polycrystals

To investigate the effect of crystallographic orientation on the polycrystalline scale, RVE with 500 grains were analyzed under identical boundary and loading conditions. In this section, it is aimed to determine how the orientation-dependent behavior observed in polycrystals evolves when grain interactions and boundary constraints are introduced.

For the 500-grain RVE, four representative crystallographic orientations with the Euler angles of $(324^\circ, 108^\circ, 98^\circ)$, $(0^\circ, 45^\circ, 45^\circ)$, $(0^\circ, 55^\circ, 45^\circ)$, and $(0^\circ, 75^\circ, 45^\circ)$ were selected based on the single-crystal results. To preserve these target orientations as the mean values, $\pm 4^\circ$ standard deviation was applied only to the second, Φ , and third, ϕ_2 , Euler angles. These angles control how the slip planes and slip directions are positioned relative to the loading axis. The first Euler angle, ϕ_1 , was kept fixed, since rotation about the loading axis does not affect the response under uniaxial compression. This procedure introduces controlled orientation variability while preventing the RVE from behaving like an effectively single crystal and yields a more realistic distribution of grain orientation. The corresponding true stress–true strain curves, shown in Figure 5.3-8, indicate that the orientation-dependent trend observed in the single-crystal simulations is preserved. The Euler angle of $(324^\circ, 108^\circ, 98^\circ)$ shows the lowest yield and flow stress, the Euler angles of $(0^\circ, 45^\circ, 45^\circ)$ and $(0^\circ, 75^\circ, 45^\circ)$ fall in an intermediate stress range, and the Euler angle of $(0^\circ, 55^\circ, 45^\circ)$ orientation exhibits the highest stress levels throughout deformation.

The quantitative results and the corresponding true stresses at 10% strain are summarized in Table 5.3-4, providing a direct numerical comparison of the trends observed in the stress–strain curves in Fig. 5.3-8 to be evaluated in a consistent manner.

Figure 5.3-9 presents the total accumulated slip (γ) contours for all twelve $\{111\}\langle 110\rangle$ slip systems in the Euler angle of $(0^\circ, 45^\circ, 45^\circ)$ orientation. Similar to the single grain case, pronounced slip localization is observed in slip systems (d), (f),

(g), and (h), while others remain less active, confirming that deformation occurs through multiple, simultaneously activated slip systems.

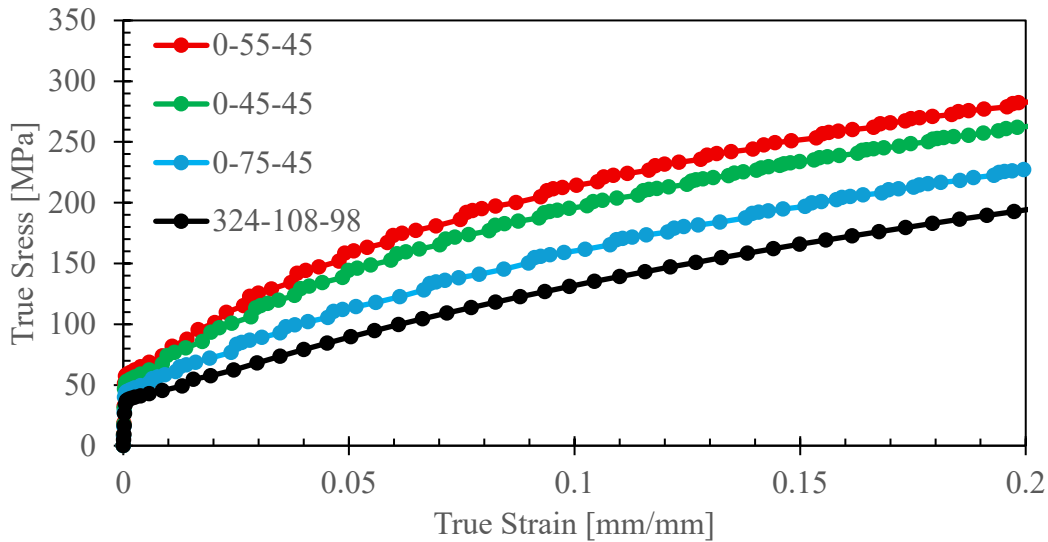


Figure 5.3-8 True stress–true strain curves for different Euler angles for 500 Grains polycrystal

Table 5.3-4 True stress-strain at 10% strain for different Euler Bunge Angles

Euler Angle	Max Schmid Factor	True Stress at 10% Strain [MPa]
0-55-45	0.28	235.53
0-45-45	0.35	215.55
0-75-45	0.43	160.16
324-108-98	0.49	131.80

In summary, in the polycrystalline simulations, higher overall stress levels are observed compared to their single-crystal counterparts, reflecting the additional strengthening introduced by intergranular constraints and grain boundary interactions. However, the $\pm 4^\circ$ orientation variability within each case also contributes to minor stress fluctuations, making it difficult to isolate purely

orientation-driven effects. A more detailed interpretation of grain orientation and grain size is addressed in the following subsection on their coupling behavior.

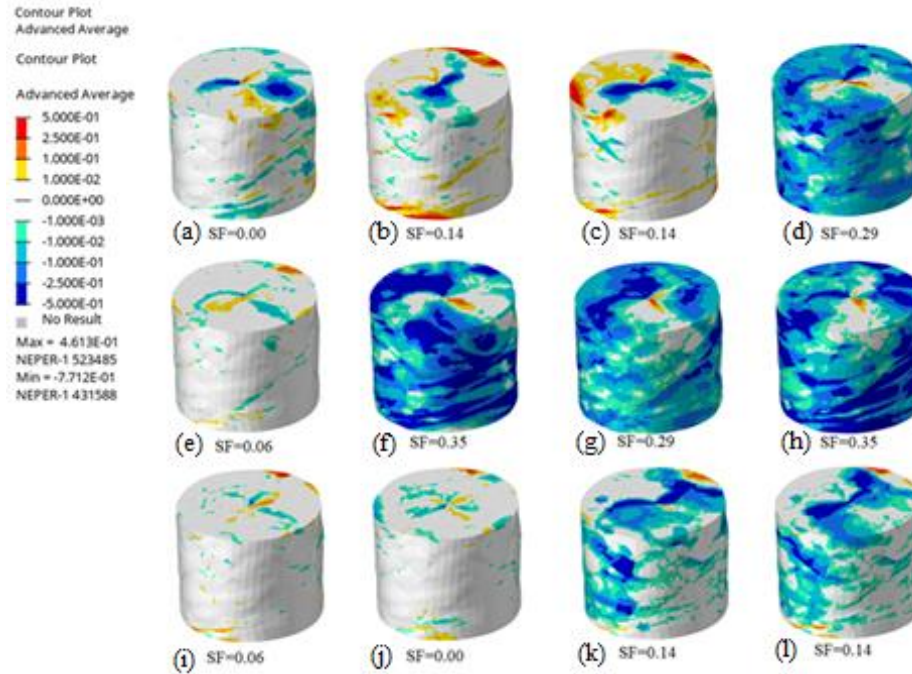


Figure 5.3-9 Total accumulated slip (γ) contours for all twelve $\{111\}\langle 110 \rangle$ slip systems, (a) to (l), in $(0^\circ, 45^\circ, 45^\circ)$ for polycrystal

5.4 Coupled Effect of Orientation and Grain Size Variation

5.4.1 Grain Set Generation

Three orientation distributions, Set B, C, D, were introduced around the Euler angle of $(324^\circ, 108^\circ, 98^\circ)$. It is shown that this Euler angle exhibits lower overall stress levels amongst other selected Euler angles. Identified same procedure in previous sub-chapter was applied to each orientation set such that the mean Euler angles of all grains corresponded precisely to $(324^\circ, 108^\circ, 98^\circ)$ as follows: Only to the second, Φ , and third, ϕ_2 , Euler angles were varied accordingly. The first Euler angle, ϕ_1 , was kept fixed, since rotation about the loading axis does not affect the response under

uniaxial compression. Variation magnitudes for each set are as follows for both Φ and ϕ_2 angles:

- Set B: $\pm 10^\circ$ standard deviation,
- Set C: $\pm 20^\circ$ standard deviation, representing moderate orientation scatter,
- Set D: $\pm 50^\circ$ standard deviation, representing a highly dispersed texture.

The 500-grain histograms in Figure 5.4-1 provide a view of distributions of the maximum Schmid factor for each grain. In the histogram, max Schmid factors are grouped for $\sigma = 10^\circ, 20^\circ$ and 50° orientations set. Visual inspection alone does not provide a reliable basis for determining whether these differences reflect systematic shifts or simple sampling fluctuations. For this reason, a statistical assessment was conducted to evaluate whether the observed variations arise from differences in the underlying populations.

A one-way analysis of variance (ANOVA) was first used for 500 grains variations to test for an overall difference among the group means of maximum Schmid factors. ANOVA evaluates the ratio of the variance between the group means to the variance within the groups. When the F-statistics exceeds the corresponding critical value from the F-distribution, the between-group variability is interpreted as larger than what would be expected from sampling noise alone. In the present analysis, $F = 8.47$, which is greater than the critical threshold ($F_{\text{critical}} = 3.00, \alpha = 0.05$). This result indicates that the three orientation sets do not share a common mean maximum Schmid factor. The associated p-value (2.19×10^{-4}) represents the probability of observing an F-statistic at least as large as 8.47 if all population means were equal. This value is well below the significance threshold. Therefore, the datasets generated with $\sigma = 10^\circ, 20^\circ$, and 50° do not originate from populations with identical mean maximum Schmid factors [30]. Since ANOVA only identifies that at least one difference exists, pairwise comparisons were performed for 500 grains using Welch's two-sample t-test, which does not assume equal variances. Two comparisons were evaluated ($\sigma = 10^\circ$ vs 20° and $\sigma = 10^\circ$ vs 50°) using a Bonferroni-

adjusted threshold of $\alpha = 0.025$. The results show that although for $\sigma = 10^\circ$ vs 20° , $p = 0.014$ is close but lower than the threshold, while for $\sigma = 10^\circ$ vs 50° the value of $p = 2.84 \times 10^{-5}$ is statistically significant.

For 50 grains with the $\sigma = 10^\circ$, 20° , and 50° orientation sets, again one-way ANOVA was performed to evaluate whether the mean maximum Schmid factors differ across the three groups. The test produced $F = 4.57$, which exceeds the corresponding critical value ($F_{\text{critical}} = 3.06$, $\alpha = 0.05$). The associated p-value (0.0109) is below the significance threshold, indicating that the three groups do not share a common population mean. The 50-grain histograms in Figure 5.4-2 display greater statistical variability due to the reduced grain count.

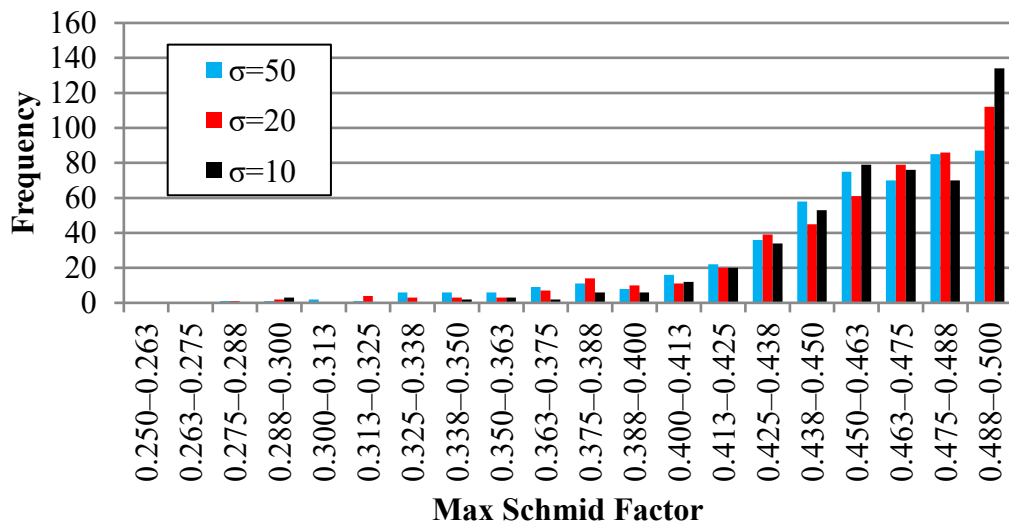


Figure 5.4-1 Max Schmid Factor histograms for three different standard deviation for 500 grains

Pairwise comparisons were then conducted for 50 grains using Welch's two-sample t-test with a Bonferroni-adjusted significance level of $\alpha = 0.025$ for the two comparisons. Both tests yielded statistically significant differences. The comparison between $\sigma = 10^\circ$ and $\sigma = 20^\circ$ resulted in $p = 0.0122$ is again close to the threshold, whereas the comparison between $\sigma = 10^\circ$ and $\sigma = 50^\circ$ produced $p = 0.0040$, significantly less compared to threshold $\alpha = 0.025$.

5.4.2 Comparative Analysis Between $\pm 10^\circ$ and $\pm 20^\circ$

The true stress–true strain curves for $\pm 10^\circ$ and $\pm 20^\circ$ standard deviations are shown in Figure 5.4-3. with the corresponding numerical results summarized in Table 5.4 - 1. A magnified view of the 20% strain region is provided in the lower-right corner of Figure 5.4-3 to highlight the stress differences between the compared curves.

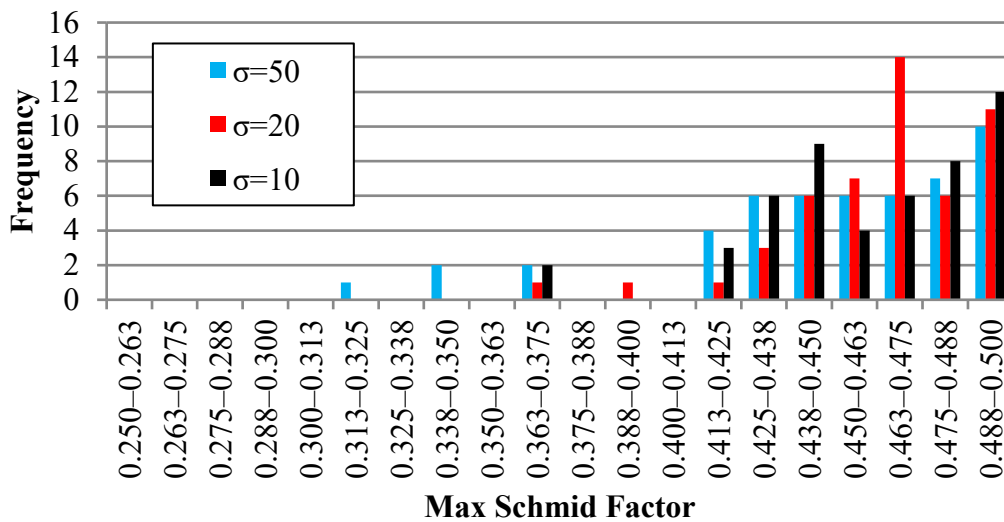


Figure 5.4-2 Max Schmid Factor histograms for three different standard deviation for 50 grains

Two aggregates with different grain counts were analyzed to evaluate how the comparison between the $\pm 10^\circ$ (Set B) and $\pm 20^\circ$ (Set C) orientation spreads affects the macroscopic mechanical response. As presented in Table 5.4-1, at 20% strain, the true stress rises from 210.93 MPa to 220.20 MPa in the 50-grain RVE, corresponding to a difference of 9.27 MPa or a 4.39% increase in flow stress. In the 500-grain RVE, the same comparison yields a stress increase from 223.84 MPa to 232.10 MPa, corresponding to an 8.26 MPa difference and a 3.69% variation.

Although both aggregates show slightly higher stresses for the $\pm 20^\circ$ set, the magnitude of the change is not drastic. This is consistent with the statistical results: for both 50-grain and 500-grain datasets, the p-values obtained from the Welch t-test

lie close to the Bonferroni-adjusted significance threshold of $\alpha = 0.025$. Consequently, the response difference between $\pm 10^\circ$ and $\pm 20^\circ$ is detectable but remains modest, and neither the tables nor the stress–strain curves exhibit a explicit separation between the two curves. This limited variation suggests that assessing the orientation scatter from $\pm 10^\circ$ to $\pm 20^\circ$ result only in smaller change the macroscopic deformation behavior.

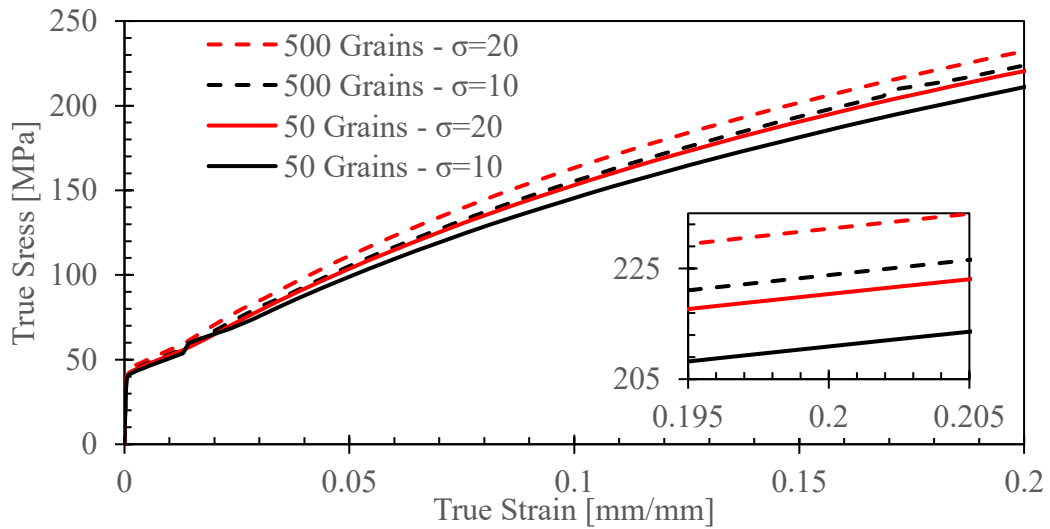


Figure 5.4-3 True stress–true strain curves for $\pm 10^\circ$ and $\pm 20^\circ$ standard deviations

Table 5.4-1 Comparative analysis of 50 and 500 Grains for $\pm 10^\circ$ and $\pm 20^\circ$ standard deviations

Set	50 Grain		500 Grain	
	$\sigma = 10$	$\sigma = 20$	$\sigma = 10$	$\sigma = 20$
Stress at %20 Strain [MPa]	210.93	220.2	223.84	232.1
Difference [MPa]	9.27		8.26	
Variation [%]	4.39		3.69	

5.4.3 Comparative Analysis Between $\pm 10^\circ$ and $\pm 50^\circ$

The true stress–true strain curves for $\pm 10^\circ$ and $\pm 50^\circ$ standard deviations are shown in Figure 5.4-4, with the corresponding numerical results summarized in Table 5.4-

2. A magnified view of the 20% strain region is provided in the lower-right corner of Figure 5.4-4 to highlight the stress differences between the compared curves.

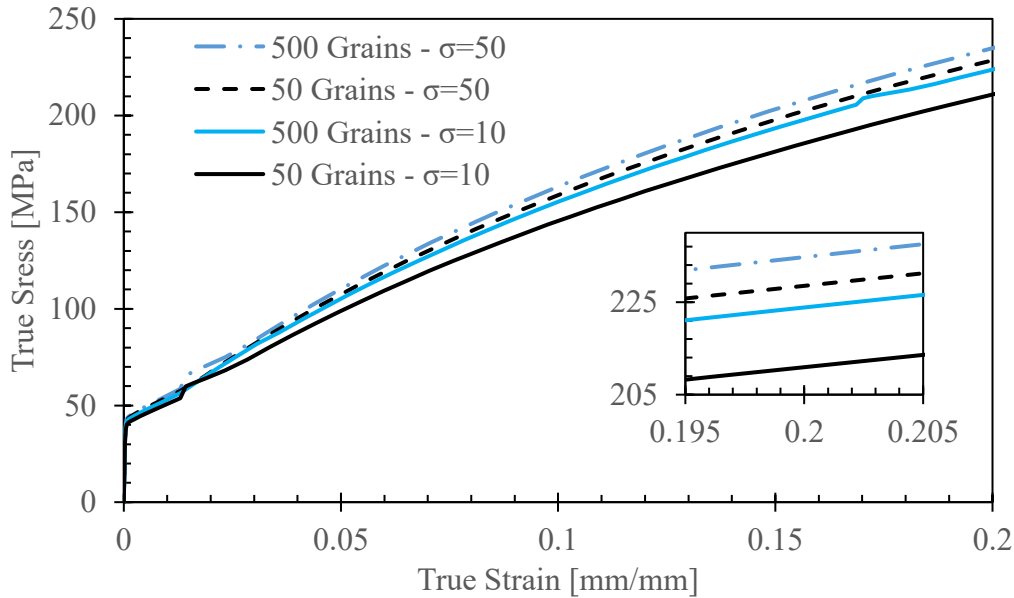


Figure 5.4-4 True stress–true strain curves for $\pm 10^\circ$ and $\pm 50^\circ$ standard deviations

A more significant effect appears when the orientation variation is increased to $\pm 50^\circ$ (Set D), as summarized in Table 5.4-2. At 20% strain, the true stress in the 50-grain RVE increases from 210.93 MPa ($\pm 10^\circ$) to 228.55 MPa ($\pm 50^\circ$), corresponding to a difference of 17.62 MPa and an 8.35% rise in flow stress. The 500-grain RVE exhibits the same trend, although with a smaller magnitude: the stress increases from 223.84 MPa to 234.76 MPa, producing a 10.92 MPa difference and a 4.88% variation. Unlike the $\pm 10^\circ$ vs $\pm 20^\circ$ comparison, where the change was modest and the p-values were close to the Bonferroni-adjusted threshold, the $\pm 10^\circ$ vs $\pm 50^\circ$ case shows a clearer and statistically reliable effect. For both the 50-grain and 500-grain datasets, the Welch t-test yielded p-values far below the significance level of $\alpha = 0.025$, indicating that the shift in orientation variation produces a meaningful change in the macroscopic response. The numerical differences in Table 5.-2 and the visible separation in the stress–strain curves are consistent with this outcome.

The comparison between the 50-grain and 500-grain RVEs shows that grain size affects how orientation variation is transferred to the macroscopic response. In the 50-grain model, the smaller grain count, high grain size, limits statistical averaging, and the macroscopic stress reflects orientation deviations more directly. In the 500-grain RVE, the larger number of grains, smaller grain size, increases averaging and redistribution, and the macroscopic response becomes less sensitive to individual orientations. This difference is observed in the reduction of the variation from 8.35% to 4.88%. Overall, the $\pm 10^\circ$ to $\pm 50^\circ$ comparison indicates that orientation variation influences the aggregate response and that the extent of this influence depends on the size of the representative volume.

Table 5.4-2 Comparative analysis of 50 and 500 Grains for $\pm 10^\circ$ and $\pm 50^\circ$ standard deviations

Set	50 Grain		500 Grain	
	$\sigma = 10$	$\sigma = 50$	$\sigma = 10$	$\sigma = 50$
Stress at %20 Strain [MPa]	210.93	228.55	223.84	234.76
Difference [MPa]	17.62		10.92	
Variation [%]	8.35		4.88	

5.5 Central Grain Orientation Effects

The local and macroscopic mechanical response of polycrystalline aggregates was examined using an additional configuration. Set A was constructed to quantify the effect of a controlled change in the central-grain orientation. In this setup, grain orientations were generated with $\pm 4^\circ$ standard deviation around the reference Euler angle of $(324^\circ, 108^\circ, 98^\circ)$. Four representative volume elements (RVEs) containing 50 and 500 grains were generated under identical boundaries and loading conditions. In each RVE, the central grain was assigned either the reference Euler angle of $(324^\circ, 108^\circ, 98^\circ)$ or the Euler angle of $(0^\circ, 45^\circ, 45^\circ)$, while all surrounding grains followed the Set A statistical distribution. This configuration was designed to examine how

the influence of a single central grain varies with grain count, grain size, by assigning two different Euler angles to the central grain while keeping the surrounding orientation distribution unchanged.

The statistical distribution of maximum Schmid factor values for the Set A configurations is presented in Figures 5.5-1 and 5.5-2. For the 500-grain RVE, the histogram shows that the majority of grains have maximum Schmid factors exceeding 0.475. Compared to the broader distributions observed for Sets B ($\pm 10^\circ$), C ($\pm 20^\circ$) and D ($\pm 50^\circ$), Set A shows a distribution concentrated near higher Schmid factor values, leading to lower yield and flow stress in the mechanical response.

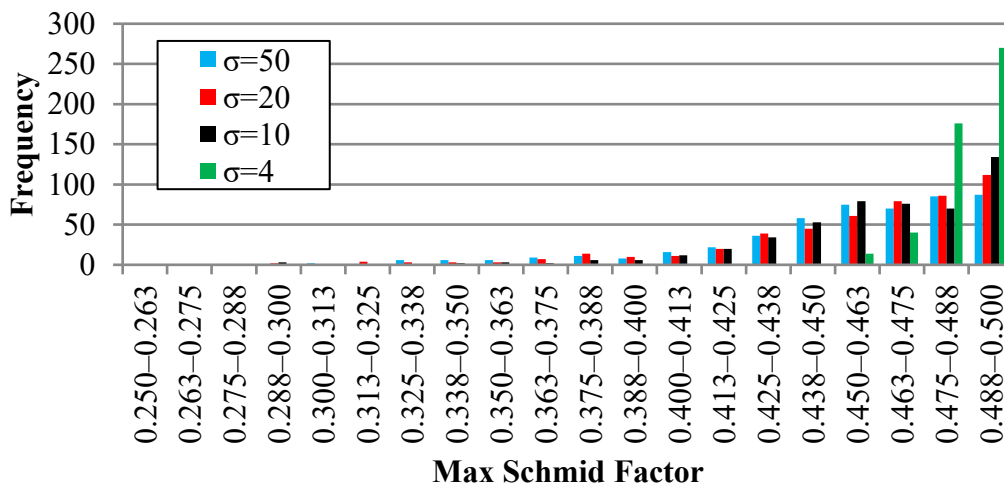


Figure 5.5-1 Max Schmid Factor histograms for four different standard deviation for 500 grains

Similarly, the 50-grain Set A histogram displays a highly concentrated distribution, with nearly 90% of the grains exhibiting maximum Schmid factors greater than 0.475. Although minor statistical fluctuations are visible due to the smaller sample size, the overall trend remains consistent with the 500-grain case. The overall geometries of the 50- and 500-grain RVEs are presented in Figure 5.5-3, where the location of central grain is identified with cursors for clarity.

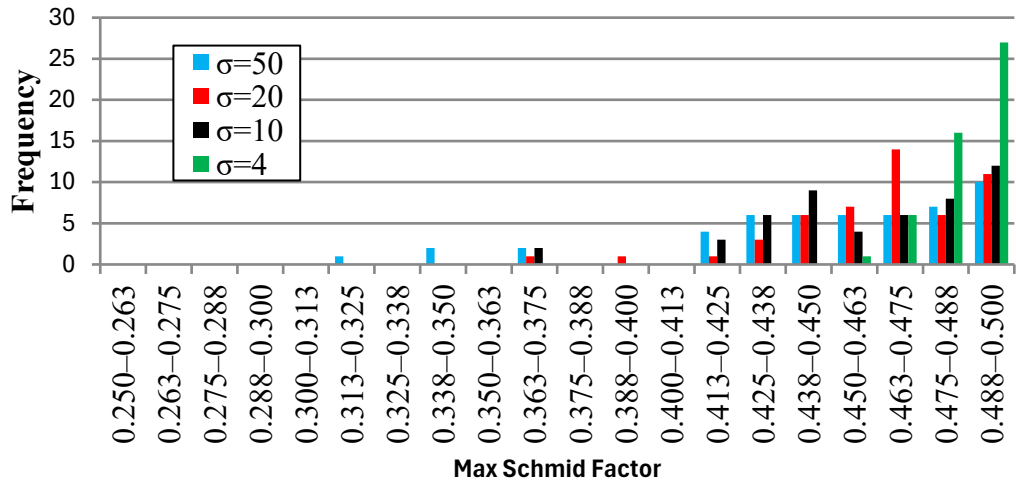


Figure 5.5-2 Max Schmid Factor histograms for four different standard deviation for 50 grains

5.5.1 Central Grain Orientation for 50 Grain RVE Results

In the 50-grain model, assigning the Euler angle of $(0^\circ, 45^\circ, 45^\circ)$ to the central grain produced elevated local von Mises stress values and distinct gradients along the grain boundaries. The corresponding plastic equivalent strain (PEEQ) contours showed localized plastic deformation around the central grain in Fig. 5.5-4. This behavior arises because the Euler angle of $(0^\circ, 45^\circ, 45^\circ)$ develops higher resolved shear resistance, leading to increased yield stress and flow stress under the applied loading, compared to the $(324^\circ, 108^\circ, 98^\circ)$ orientation. When the central grain was instead assigned to the Euler angle $(324^\circ, 108^\circ, 98^\circ)$, the stress level decreased and plastic deformation was distributed more evenly within the central grain and into neighboring grains. The arrows in Fig. 5.5-4 indicate the regions where local strain intensification was observed for the $(0^\circ, 45^\circ, 45^\circ)$ case and, in contrary, more uniform distribution was observed $(324^\circ, 108^\circ, 98^\circ)$ case.

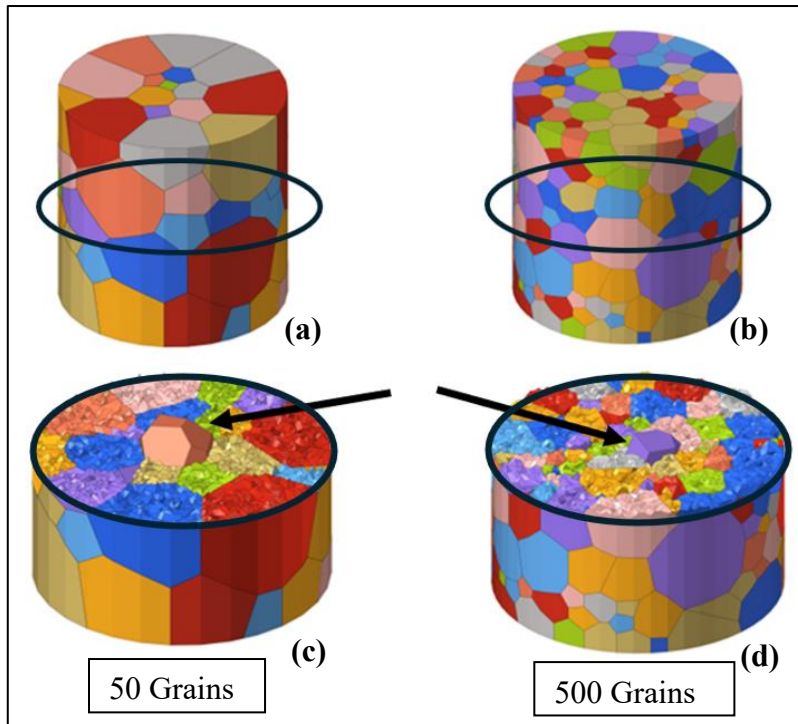


Figure 5.5-3 The overall geometries of the 50 (a), (c) and 500 (b), (d) grain RVEs

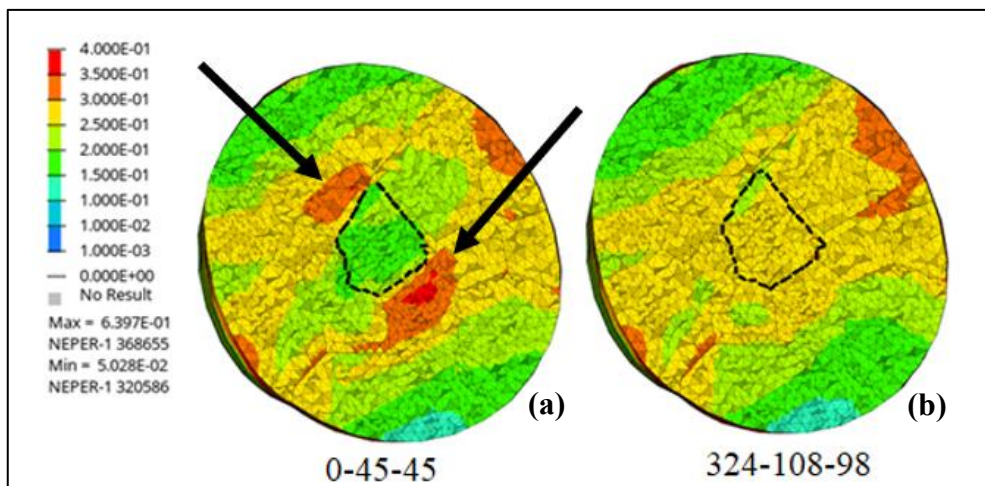


Figure 5.5-4 Section view cut through central grain shows total equivalent plastic strain contours for $(0^\circ, 45^\circ, 45^\circ)$, (a) and $(324^\circ, 108^\circ, 98^\circ)$, (b) orientations for 50 grains. Arrows show significant local strain differences.

Even in full volume Figure 5.5-5, unsanctioned visualization, the central grain exhibited a visible influence on the surrounding strain field highlighted with dashed

line, indicating that local orientation can disturb the macro-mechanical response over multiple grain boundaries.

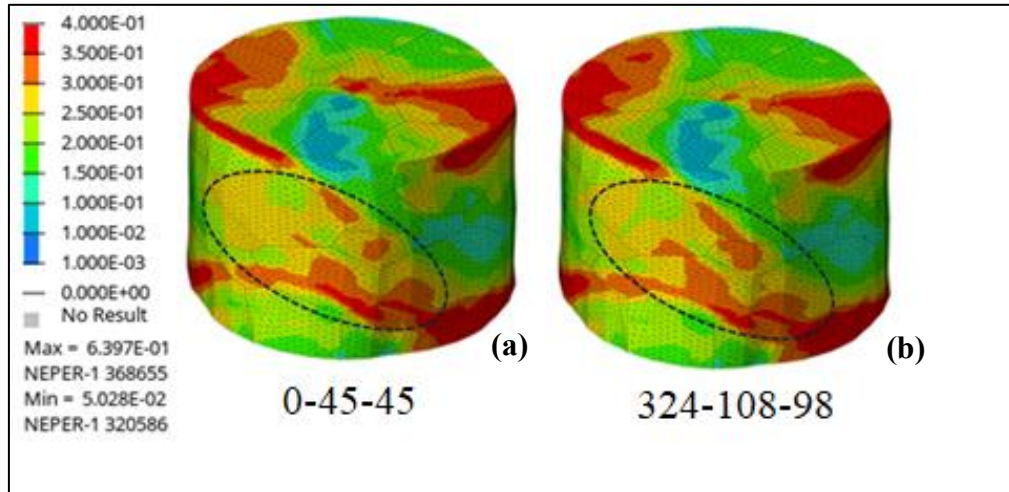


Figure 5.5-5 Full volume view shows total equivalent plastic strain contours for $(0^\circ, 45^\circ, 45^\circ)$, (a) and $(324^\circ, 108^\circ, 98^\circ)$, (b) orientations for 50 grains

Figure 5.5-6 presents the von Mises stress contours for the central grain orientation cases within the Set A configuration. The grain oriented at Euler angles $(0^\circ, 45^\circ, 45^\circ)$ exhibits stress localization, with elevated von Mises stress values concentrated along intragranular slip bands and grain boundaries. This indicates limited compatibility between active slip systems and neighboring grains, resulting in enhanced local constraint. In contrast, the Euler angle of $(324^\circ, 108^\circ, 98^\circ)$ orientation demonstrates a far more uniform stress distribution across the grain interior, reflecting smoother slip accommodation and more efficient stress relaxation due to favorable crystallographic alignment with the applied loading direction.

5.5.2 Central Grain Orientation for 500 Grains RVE Results

In figure 5.5-7, Section-view strain contours can be seen for the 500-grain RVE. The equivalent plastic strain (PEEQ) field shows that deformation is distributed across many grains with limited local variations. When the central grain is assigned to the Euler angle of $(0^\circ, 45^\circ, 45^\circ)$ orientation, slightly higher strain develops along its

grain boundaries due to reduced slip compatibility. Moreover, these higher strain regions are highlighted in Fig. 5.5-7 with arrows. When the central grain is assigned to Euler angles of $(324^\circ, 108^\circ, 98^\circ)$, strain distributes more uniformly across the grain interior and into neighboring grains. Overall, the 500-grain results indicate that the influence of a single grain on the surrounding strain field is reduced in larger aggregates.

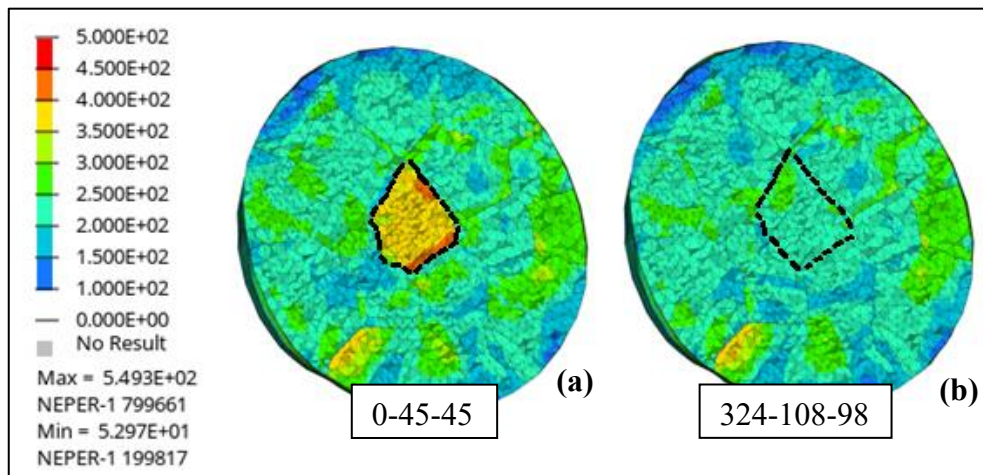


Figure 5.5-6 Section view cut through central grain shows Von Mises stress contours for $(0^\circ, 45^\circ, 45^\circ)$, (a) and $(324^\circ, 108^\circ, 98^\circ)$, (b) orientations for 50 grains

In the unsectioned strain contour Fig. 5.5-8, the macroscopic deformation pattern appears uniform across the specimen surface. The differences between the two central-grain orientations are nearly indistinguishable in this global view, suggesting that the presence of 500 grains provides sufficient statistical averaging to homogenize the mechanical response. While local variations still exist at the microscale, their projection onto the specimen surface produces only minimal contrast in the overall PEEQ distribution. This confirms that, at this scale, the mechanical fields start to be largely insensitive to isolated orientation deviations within the aggregate.

The section-view Fig. 5.5-9, von Mises stress contours provides additional information on the internal stress distribution. For the Euler angles of $(0^\circ, 45^\circ, 45^\circ)$ orientation, localized stress concentrations occur along the central grain boundaries

and at points where multiple boundaries meet. For the Euler angles of $(324^\circ, 108^\circ, 98^\circ)$, the stress field remains more uniform, with smaller gradients across the grain interior. The overall magnitude of these variations is lower than in the 50-grain case, indicating that increasing the grain count enhances the redistribution of stress across the aggregate and limits localized stress buildup.

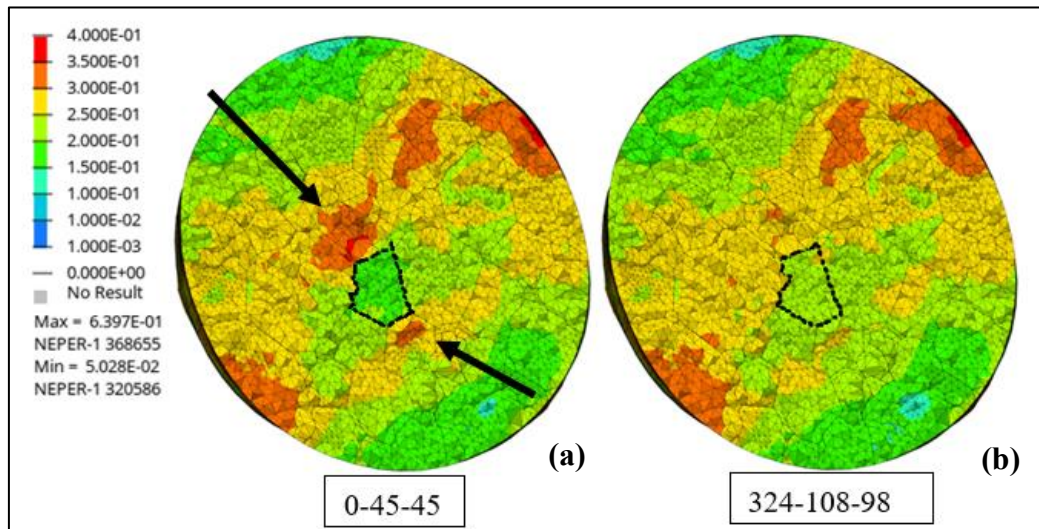


Figure 5.5-7 Section view cutted through central grain shows total equivalent plastic strain contours for $(0^\circ, 45^\circ, 45^\circ)$, (a) and $(324^\circ, 108^\circ, 98^\circ)$, (b) orientations for 500 grains. Arrows show significant local strain differences.

In the 500-grain RVE, the mechanical response shows limited sensitivity to the central grain orientation. The $(324^\circ, 108^\circ, 98^\circ)$ case develops higher resolved shear stress on its main slip systems, leading to earlier plastic activation and a more uniform distribution of strain and stress across neighboring grains. The $(0^\circ, 45^\circ, 45^\circ)$ case requires higher yield and flow stress, producing localized strain and stress variations, but these remain restricted due to the larger number of grains participating in deformation. As a result, the influence of a single grain is strongly reduced compared to the 50-grain model.

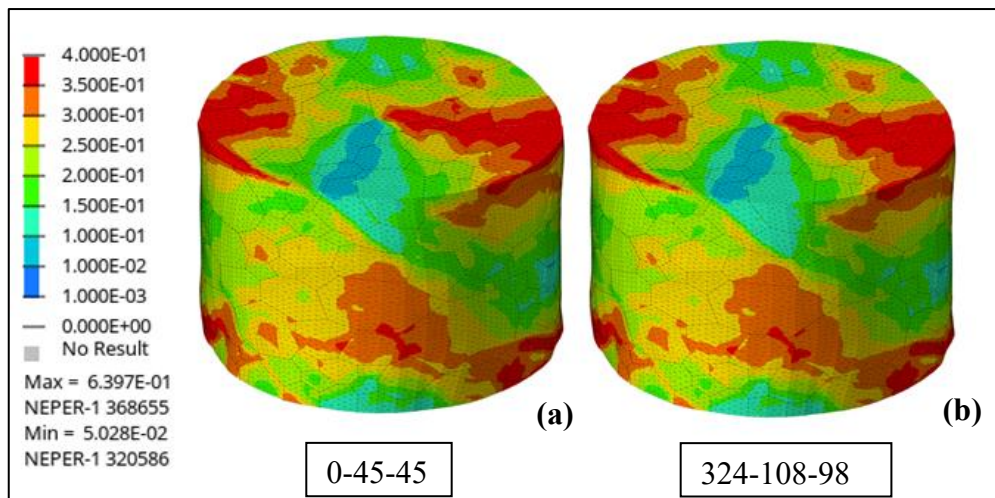


Figure 5.5-8 Full volume view shows total equivalent plastic strain contours for $(0^\circ, 45^\circ, 45^\circ)$, (a) and $(324^\circ, 108^\circ, 98^\circ)$, (b) orientations for 500 grains

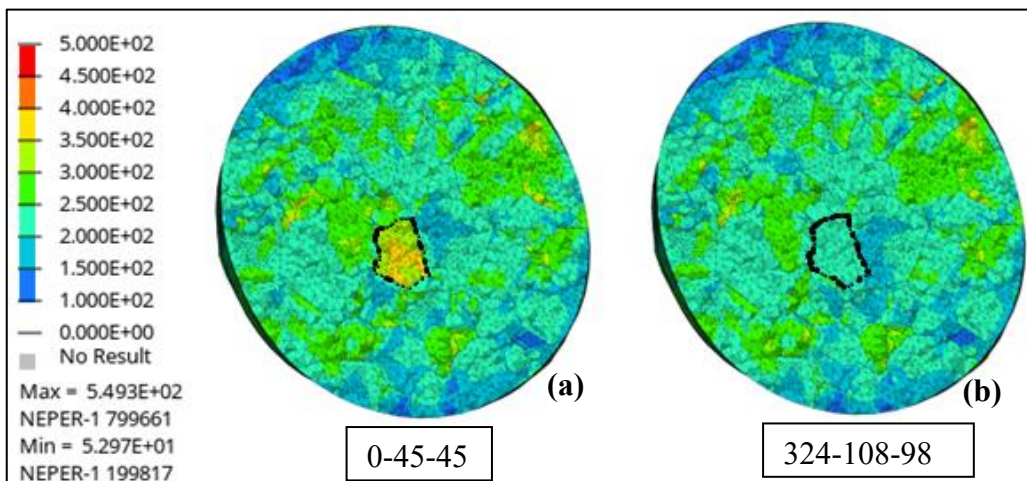


Figure 5.5-9 Section view cut through central grain shows Von Mises stress contours for $(0^\circ, 45^\circ, 45^\circ)$, (a) and $(324^\circ, 108^\circ, 98^\circ)$, (b) orientations for 500 grains

5.5.3 Comparison of Affected Regions 50 vs 500 Grains

Fig. 5.5-11 compares how the central grain affects the surrounding deformation field for both 50 and 500 grains with two cases $(0^\circ, 45^\circ, 45^\circ)$ and $(324^\circ, 108^\circ, 98^\circ)$. A dashed circular region marks the area where changes in the central-grain orientation alter the local mechanical response. In the 50-grain RVE, this region occupies a

larger portion of the total volume, and the difference between the two central-grain orientations remains visible throughout this area. In the 500-grain RVE, the same region covers a smaller part of the aggregate, and the orientation-induced differences diminish rapidly with increasing grain number, decreasing grain size.

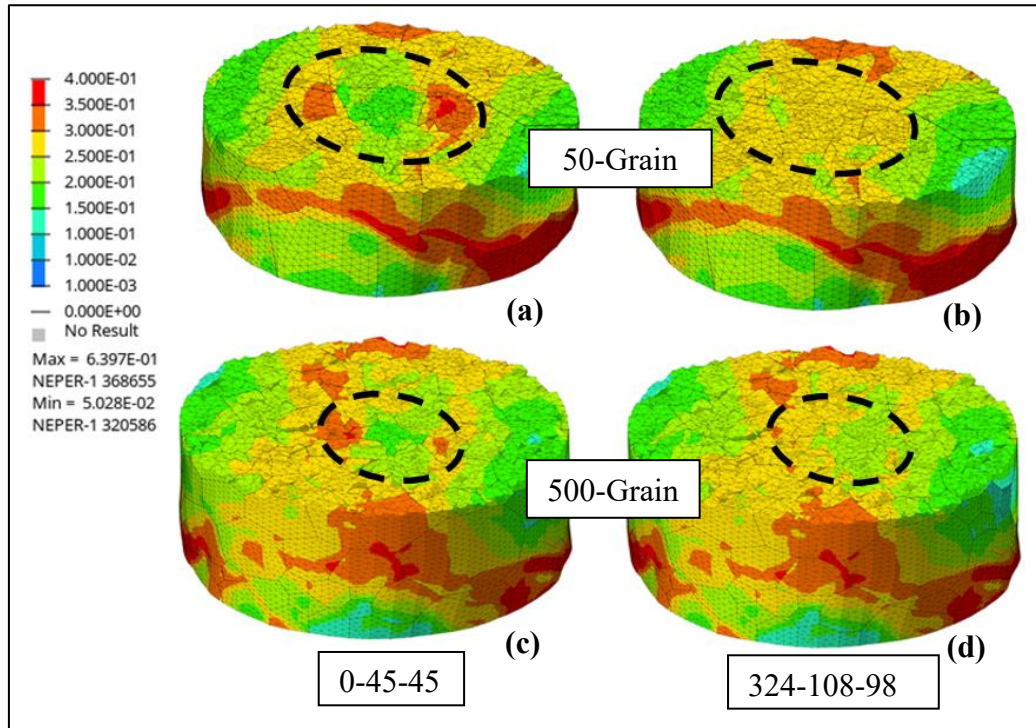


Figure 5.5-10 Section view cut through central grain shows total equivalent plastic strain contours for $(0^\circ, 45^\circ, 45^\circ)$, (a), (c) and $(324^\circ, 108^\circ, 98^\circ)$, (b), (d) orientations for 50 and 500 grains with dashed circular region centered.

The results confirm that the orientation of a single grain can influence the local mechanical fields within a polycrystalline aggregate. However, the extent of this influence is governed by the grain size within the domain. In larger grains, local orientation effects remain macroscopically visible due to limited averaging and stronger boundary constraints, whereas in the smaller grain sizes, they are dissipated through intergranular compatibility and collective load sharing.

CHAPTER 6

CONCLUSION

Through sequential studies of RVE scaling, grain orientation, grain size, and their coupled effects, the results collectively reveal how microstructural topology and crystallographic alignment govern both local and macroscopic deformation. This analysis bridges the gap between numerical reliability and physical realism, establishing a consistent modeling framework for polycrystal-scale simulations.

6.1 Grain Orientation Effects

Single-crystal simulations revealed a pronounced sensitivity of mechanical response to crystallographic alignment. The orientation, $(324^\circ, 108^\circ, 98^\circ)$, with a maximum Schmid factor of 0.49, displayed the lowest yield stress and nearly linear hardening, while the Euler angles of $(0^\circ, 55^\circ, 45^\circ)$ with a Schmid factor 0.28, exhibited higher strength and nonlinear hardening due to multi-slip activation. The rotation series from $(0^\circ, 45^\circ, 45^\circ)$ to $(0^\circ, 75^\circ, 45^\circ)$ demonstrated a monotonic increase in stress strain trend, with true stress at 10% strain increasing from ≈ 147 MPa to ≈ 244 MPa.

In polycrystalline models, the same orientations are persisted, though overall stress levels rose due to intergranular constraint. In the 500-grain RVE, the true stress at 10% strain ranged from ≈ 165 MPa for orientation $(324^\circ, 108^\circ, 98^\circ)$ to ≈ 205 MPa for orientation $(0^\circ, 55^\circ, 45^\circ)$. About a 20% increase in true stress values was observed compared to single-crystal behavior. These findings confirm that grain interaction, rather than intrinsic slip geometry alone, governs macroscopic hardening in polycrystals.

6.2 Grain Size Effect

A systematic analysis with 1, 10, 100, and 500 grains established a clear Hall–Petch-type strengthening trend. The flow stress increased from ≈ 42 MPa for the single-crystal configuration (grain size ≈ 1.8 mm) to ≈ 47 MPa for the 500-grain model (grain size ≈ 0.23 mm), while true stress at 10% strain rose from ≈ 125 MPa to ≈ 169 MPa. Strengthening saturated beyond 100 grains, indicating that the model reached a statistically representative size. The increase in boundary area and associated GND density was identified as the dominant mechanism for this behavior.

6.3 Coupled Orientation – Size Effect

Coupled orientation–size analyses using controlled orientation spreads confirmed that larger orientation variation led to higher stresses. The difference was most pronounced in the 50-grain RVE, where the limited number of grains decreased the effectiveness of statistical averaging and made orientation differences more visible in the mechanical response. In contrast, the effect was smaller in the 500-grain RVE, where a higher grain number, smaller grain size, increased homogenization across the aggregate.

6.4 Central Grain Orientation Effect

Further, the central-grain orientation analysis showed that orientation differences can change the local stress and strain fields in smaller aggregates. In the 50-grain RVE, the $(0^\circ, 45^\circ, 45^\circ)$ orientation produced localized stress variations that extended across several neighboring grains. In the 500-grain RVE, the same orientation change had a much smaller spatial reach, reflecting the increased statistical averaging associated with a larger grain count.

6.5 Overall Interpretation

The combined findings outline the governing mechanisms in crystal plasticity:

1. Orientation alignment dictates local slip activity and controls the onset and nature of hardening.
2. Polycrystalline interaction increases material strength.
3. Grain size reduction increases yield stress and plastic strength following Hall–Petch scaling.
4. Orientation variation and neighborhood constraints together define the transition from local anisotropy to global homogeneity.
5. In polycrystals, changes in the orientation of a single grain affect both the local stress–strain fields and the global response in small number of grains, while its effect is reduced in larger number of grains..

In conclusion, the mechanical response of polycrystalline copper arises from a delicate balance between crystallographic anisotropy and intergranular compatibility. The developed CPFEM framework provides numerically stable foundation for future studies of texture evolution, hardening behavior, and strain localization in FCC materials.

6.6 Future Work

Building on the findings of this thesis, several key directions are proposed to enhance predictive capability of the developed CPFEM framework.

First, grain boundary behavior could be modeled explicitly using a Cohesive Zone Model (CZM) formulation. In the current work, grain boundaries were assumed to be perfectly bonded, neglecting local decohesion or slip incompatibility. Implementing CZM interfaces would allow detailed examination of grain boundary

separation, slip transfer resistance, and intergranular damage initiation, enabling a more complete understanding of deformation and failure at the mesoscale.

Second, future studies could integrate experimentally obtained orientation data, particularly from Electron Backscatter Diffraction (EBSD) measurements. This would enable case-specific model validation against experimental stress–strain curves, ensuring that simulation predictions reflect actual microstructural textures. Such calibration would also facilitate the direct application of CPFEM in industrial process simulations and component-level predictions.

Third, the grain boundary misorientation angle could be incorporated as an independent variable. Current models capture intergranular interactions geometrically but do not explicitly distinguish between low-angle boundaries (typically $< 15^\circ$) and high-angle boundaries (typically $\geq 15^\circ$). Including misorientation-dependent constitutive behavior would make it possible to quantify slip transfer efficiency, GND accumulation, and boundary hardening mechanisms more accurately.

Finally, extending the model to account for temperature-dependent plasticity, strain-rate sensitivity, and cyclic loading would broaden its applicability to phenomena such as creep, fatigue, and thermomechanical coupling. This would enable CPFEM to predict long-term microstructural evolution and damage accumulation in copper and related FCC alloys.

In essence, future research could focus on bridging the gap between microstructural representation and mechanical fidelity, transforming the current CPFEM approach from a controlled simulation framework into a fully predictive, experimentally validated tool for advanced materials engineering.

REFERENCES

- [1] R. J. Asaro and J. R. Rice, “Strain localization in ductile single crystals,” *Journal of the Mechanics and Physics of Solids*, vol. 25, no. 5, pp. 309–338, 1977
- [2] Y. Huang, *A User-Material Subroutine Incorporating Single Crystal Plasticity in the ABAQUS Finite Element Program*. Cambridge, MA: Harvard University, 1991, pp. 1–21
- [3] J. F. Nye, “Some geometrical relations in dislocated crystals,” *Acta Metallurgica*, vol. 1, no. 2, pp. 153–162, 1953 [https://doi.org/10.1016/0001-6160\(53\)90054-6](https://doi.org/10.1016/0001-6160(53)90054-6)
- [4] A. Arsenlis and D. M. Parks, “Modeling the evolution of crystallographic dislocation density in crystal plasticity,” *Journal of the Mechanics and Physics of Solids*, vol. 50, no. 9, pp. 1979–2009, 2002; [https://doi.org/10.1016/S0022-5096\(01\)00134-X](https://doi.org/10.1016/S0022-5096(01)00134-X)
- [5] B.-B. Jung, H.-C. Park, and J.-S. Kim, “A study of micro bending test for polycrystalline thin plate,” *Proceedings of SPIE*, vol. 8344, 83441K, 2012; <https://doi.org/10.1117/12.914434>
- [6] H. D. Espinosa, B. C. Prorok, and M. Fischer, “An interpretation of size-scale plasticity in geometrically confined systems,” *Proceedings of the National Academy of Sciences (PNAS)*, vol. 102, no. 45, pp. 16933–16938, 2005; <https://doi.org/10.1073/pnas.0508572102>
- [7] T. Zhu, J. Li, A. Samanta, H. G. Kim, and S. Suresh, “Interfacial plasticity governs strain rate sensitivity and ductility in nanotwinned Cu,” *PNAS*, vol. 104, no. 9, pp. 3031–3036, 2007; <https://doi.org/10.1073/pnas.0611097104>
- [8] M. Dao, L. Lu, R. J. Asaro, J. T. M. De Hosson, and E. Ma, “Toward a quantitative understanding of mechanical behavior of nanocrystalline metals,” *Acta*

Materialia, vol. 55, no. 12, pp. 4041–4065, 2007;
<https://doi.org/10.1016/j.actamat.2007.01.038>

[9] İ. Özdemir, T. Yalcınkaya, “Strain Gradient Crystal Plasticity: Intragranular Microstructure Formation,” in *Handbook of Nonlocal Continuum Mechanics for Materials and Structures*, Springer, pp. 1-29, 2017.

[10] N. Cordero, A. I. Arias, I. Romero, and M. F. Beatty, “Micromorphic modelling of grain size effects in polycrystals,” *GAMM-Mitteilungen*, vol. 36, no. 1, pp. 1–24, 2013; <https://doi.org/10.1002/gamm.201310011>

[11] M. Lindroos, P. Heinonen, T. Alhainen, and A. Hämäläinen, “Crystal plasticity with micromorphic regularization,” *Crystals*, vol. 11, no. 8, 949, 2021; <https://doi.org/10.3390/cryst11080994>

[12] S. Haouala, J. Segurado, and J. Llorca, “Influence of grain size on the strength of FCC polycrystals via computational homogenization,” *Acta Materialia*, vol. 148, pp. 72–85, 2018; <https://doi.org/10.1016/j.actamat.2018.01.024>

[13] M. Petkov, J. Hu, and A. C. F. Cocks, “Self-consistent modelling of cyclic loading and relaxation in austenitic 316H stainless steel,” *Philosophical Magazine*, 99(7), 789–834, 2018; <https://doi.org/10.1080/14786435.2018.1556407>

[14] I.J. Beyerlein, M. Knežević, “Review of microstructure and micromechanism-based constitutive modeling of polycrystals with a low-symmetry crystal structure,” *Journal of Materials Research* 33, 3711–3738, 2018; <https://doi.org/10.1557/jmr.2018.333>

[15] E. Demir, A. M. Pecchero, C. Hardie, E. Tarleton, “OXFORD-UMAT: An efficient and versatile crystal plasticity framework *International Journal of Solids and Structures*, vol. 307, 2025, <https://doi.org/10.1016/j.ijsolstr.2024.113110>

[16] L. Mishnaevsky Jr. and S. Schmauder, “Micromechanical modelling of nanocrystalline metals,” *Computational Materials Science*, vol. 101, pp. 28–40, 2015, <https://doi.org/10.1016/j.commatsci.2014.09.024>

- [17] M. Bacca, D. R. Hayhurst, and R. M. McMeeking, “Continuous dynamic recrystallization during severe plastic deformation,” *Mechanics of Materials*, vol. 90, pp. 148–156, 2015; <https://doi.org/10.1016/j.mechmat.2015.05.008>
- [18] R. Hill and J. R. Rice, “Constitutive analysis of elastic–plastic crystals at arbitrary strain,” *Journal of the Mechanics and Physics of Solids*, vol. 20, no. 6, pp. 401–413, 1972; [https://doi.org/10.1016/0022-5096\(72\)90017-8](https://doi.org/10.1016/0022-5096(72)90017-8)
- [19] Z. C. Cordero, B. E. Knight, and C. A. Schuh, “Six decades of the Hall–Petch effect—A survey of grain-size strengthening studies on pure metals,” *International Materials Reviews*, vol. 61, no. 8, pp. 495–512, 2016; <https://doi.org/10.1080/09506608.2016.1191808>
- [20] Y. Guo, B. Chen, J. Zou, T. B. Britton, J. Jiang, and F. P. E. Dunne, “Crystal plasticity modelling and HR-DIC measurement of slip activation and strain localisation in single and oligo-crystal Ni alloys under fatigue,” *International Journal of Plasticity*, vol. 88, pp. 70–88, 2017; <https://doi.org/10.1016/j.ijplas.2016.10.001>
- [21] K. Lee, *Image-Based FE-Modelling of Electron Backscatter Diffraction for Ultrasonic Wave Propagation in Dissimilar Metal Welds*, M.S./Ph.D. thesis, 2014.
- [22] E. Schmid and W. Boas, *Kristallplastizität: Mit Besonderer Berücksichtigung der Metalle*, 1st ed. Berlin: Springer, 1935. ISBN: 978-3-662-34261-9.
- [24] W. L. Bond, “The mathematics of the physical properties of crystals,” *The Bell System Technical Journal*, vol. 22, no. 1, pp. 1–72, 1943; <https://doi.org/10.1002/j.1538-7305.1943.tb01304.x>
- [25] D. Peirce, R. I. Asaro, and A. Needleman, “Material rate dependence and localized deformation in crystalline solids,” *Acta Metallurgica*, vol. 31, no. 12, pp. 1951–1976, 1983; [https://doi.org/10.1016/0001-6160\(83\)90014-7](https://doi.org/10.1016/0001-6160(83)90014-7)

- [26] J. W. Hutchinson, “Bounds and self-consistent estimates for creep of polycrystalline materials,” *Proceedings of the Royal Society A*, vol. 348, no. 1652, pp. 101–127, 1976; <https://doi.org/10.1098/rspa.1976.0027>
- [27] R. J. Asaro, “Micromechanics of crystals and polycrystals,” *Advances in Applied Mechanics*, vol. 23, pp. 1–115, 1983; [https://doi.org/10.1016/S0065-2156\(08\)70242-4](https://doi.org/10.1016/S0065-2156(08)70242-4)
- [28] S. Das, A. Tarleton, and E. Tarleton, “Consistent determination of geometrically necessary dislocation density from simulations and experiments,” *International Journal of Plasticity*, vol. 109, pp. 18–42, 2018; <https://doi.org/10.1016/j.ijplas.2018.05.001>
- [29] Z.C. Cordero, B.E. Knight, C.A. Schuh, “Six decades of the Hall–Petch effect – a survey of grain-size strengthening studies on pure metals,” *International Materials Reviews*, vol. 61, pp. 495–512, 2016; <https://doi.org/10.1080/09506608.2016.1191808>
- [30] Y. Hochberg, & A. C. Tamhane, (1987). “Multiple comparison procedures.” John Wiley & Sons, Inc. 1987